

Lappeenranta-Lahti University of Technology LUT
School of Engineering Science
Double Degree Programme in Technical Physics

Arias-Muñoz Juan Camilo

**Characterization of irradiated and non-irradiated Low
Gain Avalanche Detectors (LGADs)**

Examiners: Prof. Panja-Riina Luukka

Prof. Erkki Lähderanta

Supervisors: Prof. Panja-Riina Luukka

M.Sc. Shudhashil Bharthuar

ABSTRACT

Lappeenranta-Lahti University of Technology LUT

School of Engineering Science

Double Degree Programme in Technical Physics

Arias-Muñoz Juan Camilo

Characterization of irradiated and non-irradiated Low Gain Avalanche Detectors (LGADs)

Master's Thesis

2021

84 pages, 55 figures, 4 tables

Examiners: Prof. Panja-Riina Luuka
Prof. Erkki Lähderanta

Keywords: LGAD, MIP, MTD, CMS, UFSD, ETL

The objective of this work was to characterize the radiation hardness of the Fondazione Bruno Kessler (FBK) Ultra-Fast Silicon Detectors (UFSD) UFSD3.2 batch by comparing their capacitance-voltage characteristics before and after hadron irradiation at different fluence values. Stability tests gave an estimate of the radiation hardness against hadron radiation and the annealing studies showed the effect of beneficial annealing on the radiation damage. Transient current technique (TCT) was utilized to determine the operability of the sensors after the irradiation, and it was also used for determining the interpad distances. Some of the results were compared with previous measurements from Hamamatsu Photonics K.K. (HPK) sensor batch and with previous measurements from FBK UFSD3.1 batch, with the objective of getting an estimate of the performance compared to sensors from another manufacturer. All measurements and related activities were carried out at the Helsinki Institute of Physics (HIP) Detector Laboratory as a member of the Compact Muon Solenoid (CMS) upgrade research group.

ACNKOWLEDGEMENTS

Doing my master's studies in Finland, working in a complete new topic for me as are silicon detectors, in a rewarding environment like the one offered at The Helsinki Institute of Physics and LUT university is a new exciting experience that was decisive in my career as a researcher. This could not have been possible without the help and support of my family. My parents Uriel and Policarpa, my sister Valeria and my beloved Tanya who sacrificed everything to give me a chance to follow my dreams in exchange for their happiness.

I want to thank first Professor Panja-Riina Luukka for taking me into her group in a moment of need and for allowing me to learn directly from the first class professionals that work at the HIP Detector Laboratory to whom I also want to thank for being so supportive and helpful while I was getting introduced to work with them. Specially I want to thank Shudhashil Bharthuar for having infinite patience while dedicatedly teaching me the essential concepts of this work. If it was not for them this thesis would not have been possible. My gratitude to Professor Erkki Lähderanta as well for giving me the chance to come to LUT and continue my career in Finland.

I want to thank also the people that was around me filling my time here with joy: Orlando Salcedo, Clara Mendoza, America Quinteros and Aleksei Mashlakov and acknowledge my mentors who introduced me into physics with perseverance and patience Sergei Aleksandrovich Rykov and Vadim Aleksandrovich Shaligin.

Lappeenranta 2021

Juan Camilo Arias Munoz

ABBREVIATIONS

3D	Three dimensional
4D	Four dimensional
ASIC	Application-specific Integrated Circuit
ATLAS	A Toroidal LHC Apparatus
BTL	Barrel Timing Layer
C-V	Capacitance - Voltage
CERN	Conseil Européen pour le Recherche Nucléaire
CMS	Compact Muon Solenoid
CNM	Centro Nacional de Microelectrónica
CzSi	Czochralski Silicon
DC	Direct Current
ECAL	Electromagnetic Calorimeter
ETL	Endcap Timing Layer
ETROC	Endcap Timing layer Read-out Chip
FBK	Fondazione Bruno Kessler
GL	Gain Layer
HCAL	Hadron Calorimeter
HIP	Helsinki Institute of Physics
HL-LHC	High-Luminosity Large Hadron Collider
HPK	Hamamatsu Photonics K.K.
IR	Infra Red
JTE	Junction Termination Edge
LGAD	Low Gain Avalanche Detector

LHC	Large Hadron Collider
LS2	Long-Shutdown 2
LS3	Long-Shutdown 3
MIP	Minimum Ionizing Particle
MTD	Minimum Ionizing Particle Timing Detector
PCB	Printed Circuit Board
PIN	P-type-Intrinsic-N-type
RMS	Root Mean Square
ROC	Read-out Chip
S/N	Signal/Noise
SCR	Space Charge Region
SiPM	Silicon Photomultiplier
SM	Standard Model
TCT	Transient Current Technique
TDC	Time-to-Digital Conversion
UFSD	Ultra-Fast Silicon Detector
W	Wafer
WF2	Weightfield 2

CONTENTS

INTRODUCTION.....	7
1. Literature review.....	8
1.1. The CMS Experiment.....	8
1.2. The CMS Silicon Tracker and the CMS Timing detector.....	12
1.2.1. The pixel detector.....	14
1.2.2. The strip detector.....	15
1.2.3. The timing detector.....	16
1.3. Energy loss and particle detection.....	20
1.4. Silicon detectors.....	25
1.4.1 Structure.....	26
1.5. Pn-junction.....	27
1.6. PIN diode.....	31
1.7. LGAD.....	32
1.7.1. Timing resolution.....	37
1.8. Radiation damage.....	38
2. Experimental methods.....	40
2.1. CV-measurements.....	42
2.2. Annealing studies.....	46
2.3. TCT-measurements.....	47
3. Results and discussion.....	48
3.1. Depletion voltage.....	48
3.2. TCT measurements.....	52
3.3. Annealing studies.....	58
3.4. Discussion.....	62
Conclusions.....	76
References.....	77

INTRODUCTION

After the advances in high-energy and particle physics achieved by the experiments at the Large Hadron Collider (LHC) at the European Organization for Nuclear Research (CERN), it is clear that the experiments have already fulfilled their original objective of identifying the Higgs boson. Moreover, they have achieved such a level of understanding the subatomic phenomena that it unlocks the ability of predicting and controlling a huge amount of processes inside the standard model (SM) of particles[1]. Identifying precisely the whole picture that known phenomena form will allow future researchers to clearly identify what is “not in the right place”, i.e. the anomalies that correspond to new physics. In order to take the next step forward, the LHC project is planning to evolve into the High-Luminosity Large Hadron Collider (HL-LHC), where higher amounts of particles per unit of time will be measured by the experiments. This translates into higher radiation fluences that new detectors must tolerate during the planned operation time of the HL-LHC.

The Compact Muon Solenoid (CMS) experiment is a detector meant for analyzing particles generated after proton-proton collisions with the help of a giant superconducting solenoid. In the high luminosity era, the fluence of particles generated after each collision will increase dramatically, making it more difficult to track and differentiate one particle from the rest. Situations when after the collision of a bunch of protons it is not possible to separate several particle trajectories or when secondary collisions occur and the data reported ends all mixed up are known as “pileup” events. In order to solve this issue, the timing detector (MTD) proposal was agreed to be implemented. This new detector layer is divided in barrel timing layer (BTL), composed of scintillating detectors, and two endcap timing layers (ETL), that will be using silicon-based low gain avalanche detectors (LGADs). Its component detectors increase the particle tracking precision and allow to identify which events happen first, giving this way another parameter to untangle pileup events: “the timing information”.

The aim of this thesis is to study the effects of radiation on the last batch of detectors produced by FBK and HPK for the CMS MTD-ETL timing detector. Qualitative comparisons will be carried out between non-irradiated, irradiated and annealed samples, and the samples are characterized by different methods to determine their stability under HL-LHC operation conditions of the CMS experiment.

1. LITERATURE REVIEW

1.1. The CMS Experiment

The CMS experiment is a general-purpose detector. It is one of the two largest experiments measuring proton-proton collisions at the most powerful particle accelerator on Earth, the LHC at CERN. The collective objective of the experiments at the LHC is to cooperatively study the events occurring at high energy collisions of accelerated particles, to reveal the physics hidden beyond the SM. The SM was completed on 2012, when a particle matching the properties of the Higgs boson was detected at the CMS and ATLAS detectors[2]. Further research in this field aims to prove proposed theoretical models for particle behavior, interaction and existence, as well as to explain the characteristics of phenomena such as dark matter through the missing energy calculation of “supersymmetric” particles generated at the collisions.

The CMS experiment consists of several detector layers placed in a compacted cylindrical space. Each layer plays a key role detecting different particles and collision characteristics. A superconducting magnet surrounds the tracking layers and the calorimeters (it is placed between the hadron calorimeter and the return yokes) [3]. This is the largest solenoid ever constructed, and with its return yokes that help to contain the magnetic field, its total weight is about 12500 tons (Figure 1). The solenoid generates a 4 T magnetic field that bends the trajectory of the charged particles after the collision. This bending allows the identification of the type of charge (or the absence of it) of the particle traversing through the detector, as well as its momentum. The information compiled by the whole set of detectors can be used to analyze the collision, its conditions and the nature of the particles originated from the collision event.

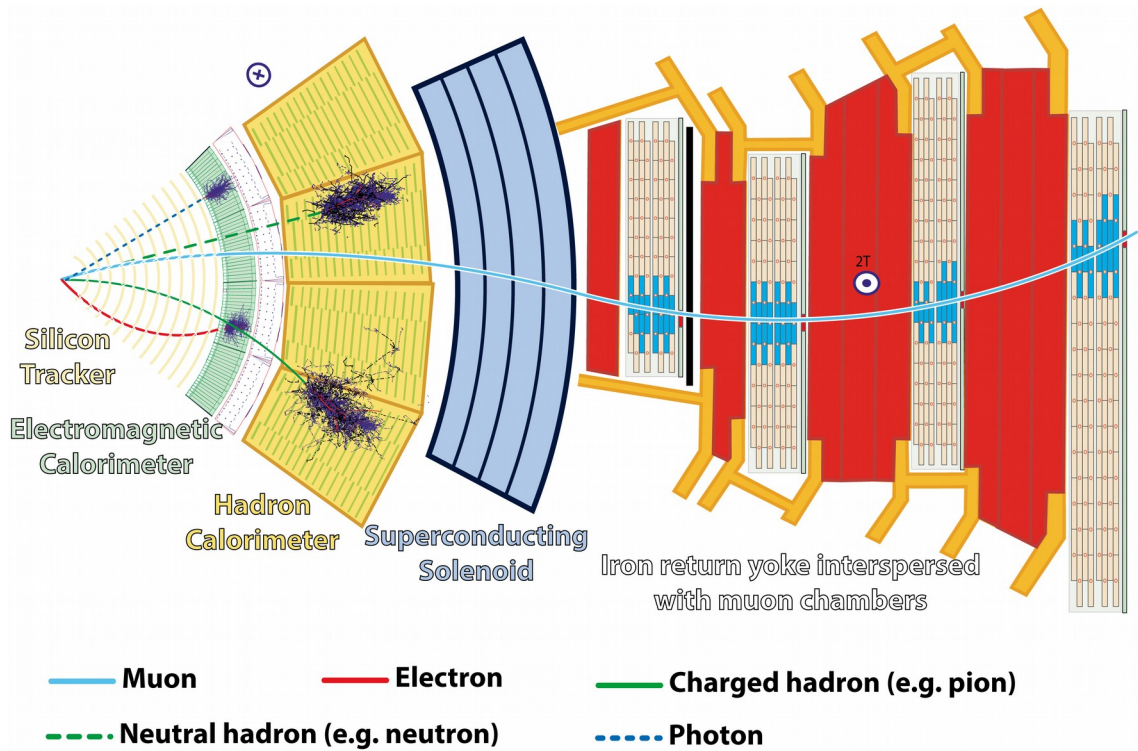


Figure 1. The different CMS detector layers, the solenoid, and a muon traversing through the detector [4].

As shown in the Figure 1. the layers and their functions are:

- The muon chambers are located outside the vacuum chamber of the solenoid and in between the return yoke layers. Muons are fermions with a mass of 200 times the mass of an electron. They can traverse the whole detector without being stopped by the calorimeters, and thus they can be used as an indication to the readout system that a collision has happened. i.e. they can be used as a trigger. The information provided from the muon chambers summarizes the hits by track stubs and the one from the calorimeters is a combination of data and energy sums that identifies the type of particle by the energy deposited. After receiving the data and after some crossings had occurred the Level-1 trigger sends a yes/no decision. Meanwhile, the data has been saved in the detector by a pipeline with the same depth than the Level-1 trigger and it remains there until the trigger decision is made. The decision depends also on the information provided by primitive triggers from each layer of the detector that after being considered by the global triggers from the muon and

calorimeter layers is transmitted to the Level-1 for the acceptance of the decision[5].

- The hadron calorimeter (HCAL) measures the energy of protons, neutrons and other types of hadrons, which are particles composed of quarks and gluons. It is mandatory to make sure that the calorimeter records every possible particle inside its structure. Doing that it can indirectly show the presence of “invisible” non-interacting uncharged particles such as neutrinos. The layers of the calorimeter are built in zigzag to make sure that no particle escapes the detector.
- As there is a calorimeter for stopping and measuring hadrons, there also has to be a calorimeter for stopping electrons and photons, which give crucial information for the identification of new particles. However, the extreme conditions and high precision requirements can be achieved only by using a very specific kind of material. The electromagnetic calorimeter (ECAL) is made of lead tungstate with oxygen addition that gives transparency and the scintillation property to the metal. The light emitted by this material comes in precise pulses that vary in intensity depending on the energy of the electrons and photons traveling through it triggering the scintillation. Preshower detectors sit before the calorimeter endcaps, closer to the collision zone, to filter high energy single photons from low energy photons that would add no useful information to the experiment results.
- Finally, the closest detector to the collision point is the Silicon Tracker. It is the layer that suffers the highest fluence of radiation, and it is responsible of the high resolution in tracking the trajectory of the particles generated at the collision events. It is divided in strip detector and pixel detector. The strip detector consists of four single-sided and two double-sided outer barrel layers with two endcaps and four inner barrel layers assembled in shells with two inner endcaps (Figure 2). The pixel detector contains about 125 million pixels, each one bump-bonded to an individual readout channel. In total, the Tracker has about 130 million individual channels. The technology that is implemented in the Tracker has been drastically changed since its first design as the concept of a radiation resistant detector and electronics was hard to define at a low cost and with the lowest weight possible to avoid disturbing the particles while they are traversing through the detector. The

particles traveling through the silicon create electron-hole pairs (around 80 e-h/ μm) that can be measured as signal current traceable with a precision of up to 10 μm .

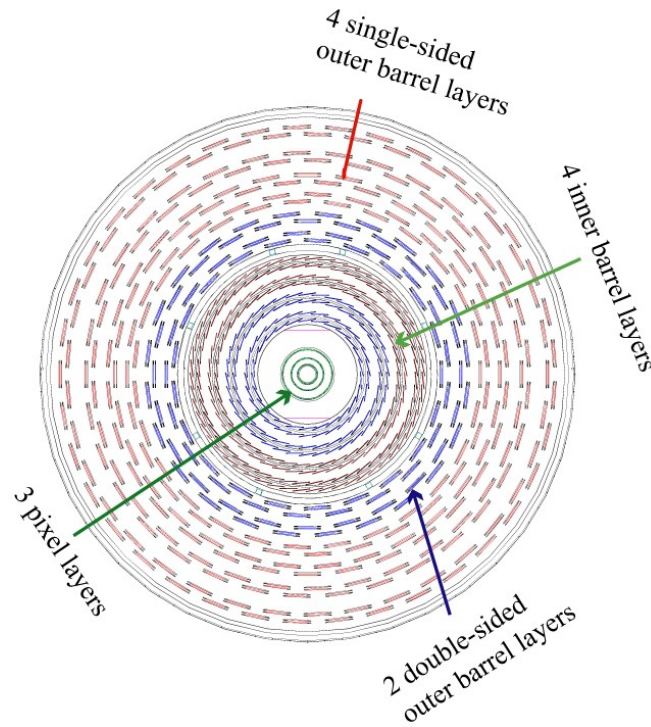


Figure 2. Representation of the CMS Silicon Tracker layers in a perpendicular to the beam view [6].

The original planning for the LHC allowed it to reach maximum collision energies of 14 TeV, but due to delays in the experiment planning, unexpected failures [7] and scheduled stops, the collision energy of the collider has been upgraded only to 13 TeV before the Long-shutdown 2 (LS2)[8]. The actual maximum collision energy value possible for the LHC is 14 TeV.

The integrated luminosity characterizes the amount of collisions that can be produced in a detector per cm^2 and per second. It is the most important parameter of an accelerator. It is expressed in inverse area units (inverse barns and femtobarns) per time and it can be interpreted as the total area of all the interactions cross-sections registered by the detector in the time established. Before LS2 the LHC had an integrated luminosity of 150 fb^{-1} , this value rose till 350 fb^{-1} and is predicted to rise again after the Long-Shutdown 3 (LS3), when the implementation of the Phase-2 CMS upgrade will be carried out (Figure 3).



Figure 3. Upgrading schedule for the LHC [9].

The luminosity inside the LHC can be expressed as:

$$L = \frac{kN^2 f \gamma}{4 \pi \beta' \epsilon} F \quad (1)$$

Here, f is the frequency of the bunches reaching the collision point, k is the amount of bunches per beam, N is the amount of protons per bunch, ϵ is the normalized emittance, β is the betatron or envelope beta function at the collision point, F is the loss from the crossing angle and γ is the Lorentz factor. Integrating this value over a time interval the integrated luminosity for this period is obtained.

The maximum collision energy allowed by the LHC design is about to be reached. By increasing the beams' transverse emittance and the frequency of the proton bunches the integrated luminosity is expected to reach values around 3000 and 4000 fb^{-1} after the LS3 is completed. Applying this upgrade, together with the implementation of a new generation of particle physics experiments, a prominent increment in the efficiency of the particle detector experiments will be achieved.

1.2. The CMS Silicon Tracker and the CMS Timing detector

The Silicon Tracker is the innermost part of the structure, thus it must tolerate the highest amount of radiation at each collision and be still able to record data with an efficient signal/noise (S/N) ratio while keeping its integrity for further measurements. The

high granularity of the detector and relatively low minimum ionizing particle (MIP) energy of silicon open the possibility to determine with high precision the path of the particles after the collision [10].

It is the ability of tracking which gives the experiment a higher resolution allowing it to identify the pass of a particle through its volume from all the noise generated inside the device. This capacity is improved significantly when the time factor is added in a four dimensional upgrade (4D) to the spatial three dimensional (3D) reconstruction of the Tracker, as co-spatial events can be detected at different moments after the collision “untangling” pileup information that used to overwhelm past generation detectors.

The Tracker is capable of handling a mean value between 20 and 30 pileup collisions per bunch of protons for pseudorapidities up to 2.4. After the next planned upgrade (Phase-2) it is expected to increase the operational range up to values between 140 and 200 pileup events for pseudorapidities up to 3 for the calorimeters and 3.8 for the Silicon Tracker (Figure 4)[11].

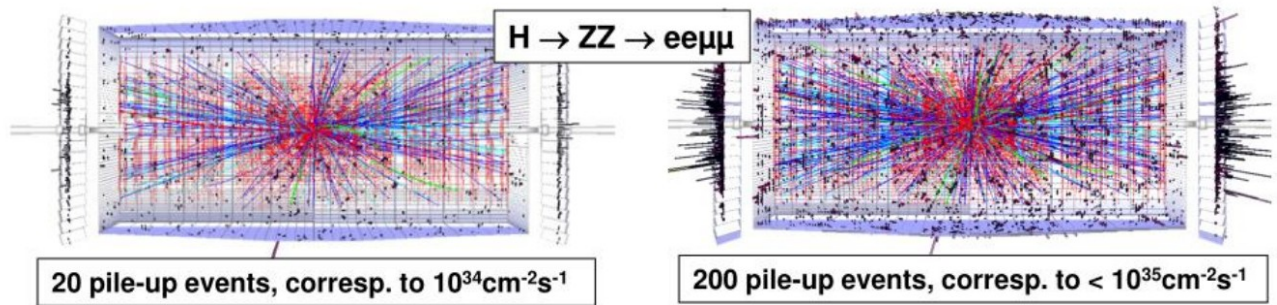


Figure 4. Representation of the increment of pileup events at expected instant luminosities for HL-LHC.[12]

The detector was installed before the LHC started operations, but has been taking data since the first collisions from the LHC. The present detector is able to work up to an integrated luminosity of 500 fb^{-1} . The Tracker is divided in pixel detector and strip detector. At the same time, the Tracker strip detector is divided in outer layer, inner layer and end caps as it was shown in Figure 2. The original detectors from the beginning of the operation of the LHC in 2008 were chosen to be fully made of silicon on December 1999. The innermost part, the pixel Tracker, consisted of pixel detectors. The barrels surrounding

it consisted of strip detectors distributed in 10 different layers whose useful life was about 10 years. In total 1440 pixel detectors and 15148 strip detectors were used [10,13].

1.2.1. The pixel detector

The pixel detector offers the 3D coordinates of the closest region to the collision point with a precision of 10 μm . It is located in the environment with the highest fluence of radiation in the experiment and it gives high-precision charged-particle tracking information and vertex reconstruction information. The original design of this detector consisted of three layers placed at 44, 73 and 102 mm from the beam pipe and four endcaps, two at each side of the interaction point at 345 and 465 mm. This design was able to work for instantaneous luminosities of $10^{34} \text{ cm}^{-2}\text{s}^{-1}$ and worked for up to 25 pileup events at 25 ns bunch time spacing. The original detector operated from 2008 to 2016 in what is known as the Phase 0 detector [14]. The Phase 0 pixel detector consisted of 66 million cells covering a total silicon area of 1.1 m^2 and was designed to be easily replaced due to expected radiation damage on the detector. One of the largest disadvantages of the Phase 0 layout was that the limited capacity of the electronics together with the severely damaged pixel detectors created dead time and inefficiencies in the measurements.

The upgrades of the accelerators on 2013 during LS1 increased the collision energy and luminosity values. This is why, between 2016 and 2017 the first Tracker upgrade took place at the Phase-1 CMS upgrade as the luminosity and average pileup events doubled their values exceeding the capacity of the Phase 0 Tracker. During this upgrade, the slow rate of electronics recording has been improved changing from 40 MHz in analogue to 160 MHz in digital. The radiation resistance has been enhanced and an extra layer has been added closer to the beam pipe as well as another endcap layer with a different design from the original turbine-like shape. Now the new radii of the pixel layers has become: 29, 68, 109 and 160 mm and the endcaps were placed at 291, 396 and 516 mm respectively. A total of 1856 modules are installed in this upgrade, each one consisting of 160×416 pixels connected to 16 read out chips (ROCs) (124 million readout channels in total). The upgraded detectors at Phase-1 are n⁺-in-n sensors, have a size of $100\mu\text{m} \times 150\mu\text{m}$ and are expected to be functional until maximum instantaneous luminosity of $2 \times 10^{34} \text{ cm}^{-2}\text{s}^{-1}$.

1.2.2. The strip detector

The strip detector consists of 15000 silicon modules covering an active detector area of 200 m². These sensors are AC-coupled p⁺-in-n single-sided microstrip detectors divided as outer and inner barrel by the 60 cm radius mark from the beam pipe. The inner barrel is equipped with four layers covered with strings of three thin modules placed inside and outside the shells of this subdetector. The outer barrel has six layers that can be equipped with three single-sided or double-sided modules on each side of the shell. Inner disks have three disks per side carrying three rings and three detector modules per ring. The endcaps of the Tracker are nine disks with v-shaped supports for 28 modules in seven rings mounted on each side of the disc and not always presenting the same geometries[10]. In total there are 10 million strips in the Strip Tracker. These 10 million strip detectors remain the same during the Phase-1 upgrade [12] and will be upgraded by the first time at Phase-2. The size of the whole Tracker during the Phase-1 slightly changed only due to the changes in the pixel detector (Figure 5).

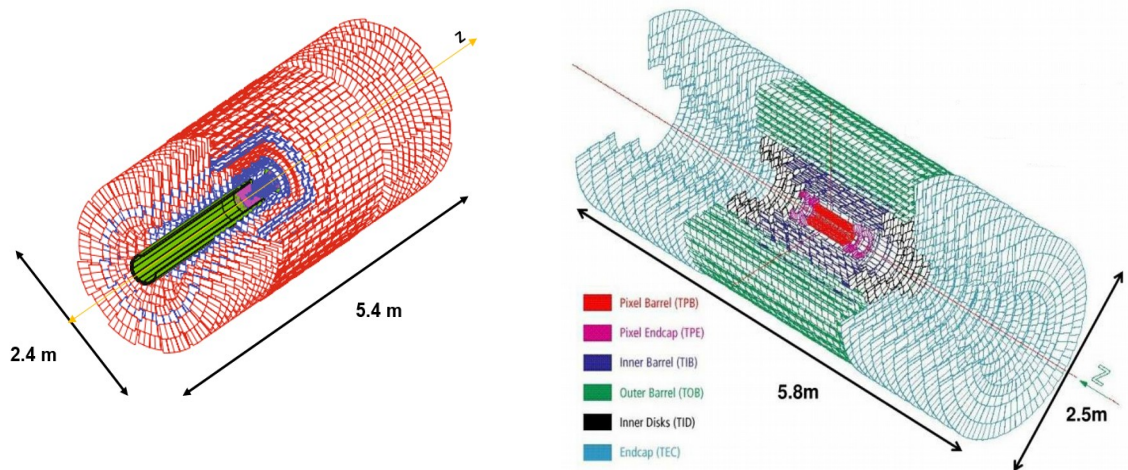


Figure 5. Silicon Tracker layout phase 0 (left), and Phase-1 (right). The separation of barrels and the upgrade of the pixel detector is clear in the upgraded version (adapted form [12] and [15]).

1.2.3. The timing detector

The next planned upgrade, the Phase-2 upgrade will include a timing detector layer that will increase the separation capacity for pileup events and identification of long-lived particles. It is based on the principle that each separated event happening inside the CMS detector has its own time for occurring. A mix of high resolution tracking with a time resolution of 30 to 40 ps (50 to 60 ps at the end of the operative life of the HL-LHC) gives the Tracker excellent identification capabilities to events happening very close to each other. The precise collision reconstruction of an event happening at a specific time allows the association of signals tightly entangled with different moments inside the time interval of the collision. Along the detector the collision events happen in a mean range of time from 180 to 200 ps and secondary collisions may happen as well.

The already approved setup for the electronics, cooling systems and the disposition of detectors must be maintained. This was in the beginning an obstacle for the design of the timing detector and only left two possible spots to place it (Figure 6): between the outer barrel of the Tracker and the electromagnetic calorimeter (ECAL) (the barrel timing layer BTL), and in the space between the bulkhead of the Tracker and the endcap calorimeter (the endcap timing layer ETL).

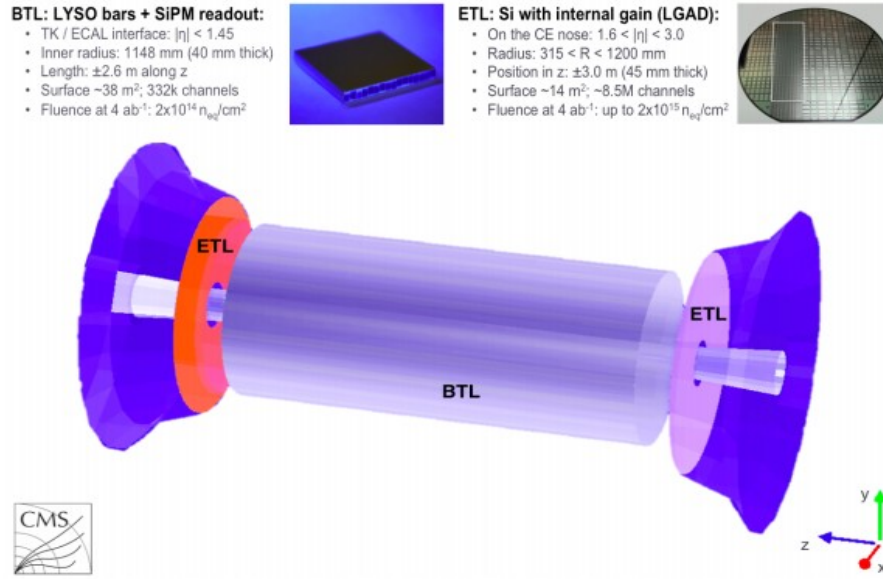


Figure 6. Timing layers schematic showing the position of the future MTD (MIP time detector) [16].

According to the 2019 CMS technical design report, factors such as mechanical constraints, radiation tolerance, costs, performance and upgrade schedule reduced the timing detector to a thin layer. The barrel layer must be placed 40 mm inwards towards the beam pipe from the inner surface of the Tracker support tube. The endcap layer will be supported between the electromagnetic calorimeter and the nose cone of the Tracker in an isolated space. However, the geometry of the space only allows the timing detector to cover pseudorapidities under a maximum of 3 while the Tracker upgrade will be able to detect particles up to a value of 4 (Figure 7)[16].

The chosen detectors for the barrel timing layer after studying several different technologies were the pixel avalanche crystal scintillator detectors that operate in Geiger breakdown mode with silicon photomultiplier (SiPM) readout electronics. In the endcap layer the most suitable technology was found to be the silicon-based LGADs that also work under avalanche principle but with a controlled gain value between 10 and 30. This work is focused solely on the LGAD detector characterization for the endcap timing layer.

LGAD two-disk systems are planned to be installed in the endcap region in a limited space of just 45 mm, 3m from both sides of the interaction region. This way, each track will generate two hits allowing a high quality timing resolution. Their radial coverage will go from 315 to 1200 mm what translates into a pseudorapidity from 1.6 up to 3, as it was shown in Figure 7.

The radiation fluence that this layer will receive is very similar in the most outer radii distances to the radiation received by the BTL. At the inner radii, the fluence value reaches levels 30 times higher than in the outer radii. Thus, it is necessary that the construction of the ETL gives access for future replacements of the sensors after heavy irradiation.

In order to keep a good resolution level in high radiation environment, the design predicted a high number of detectors covering the endcap layer. A 16x32 array of square LGAD pads, each one of 1.3x1.3 mm², meaning a total of 4x10⁶ pads per end. The modules will be connected to application specific integrated circuits (ASIC's) of 20x20 mm² capable of measuring the time of arrival and the time of threshold using the timing of leading edge of the signal pulse.

The service hybrids are innovative parts of the setup that are mounted on the detector, indicated in Figure 8 as orange bars. Their purpose is to connect the sensors with several ETL read out chips (ETROCs) and send the information to the processing unit; apply DC current and bias voltage, communicate and monitor the endcap timing readout chips with their two component boards, the readout and the power boards [16].

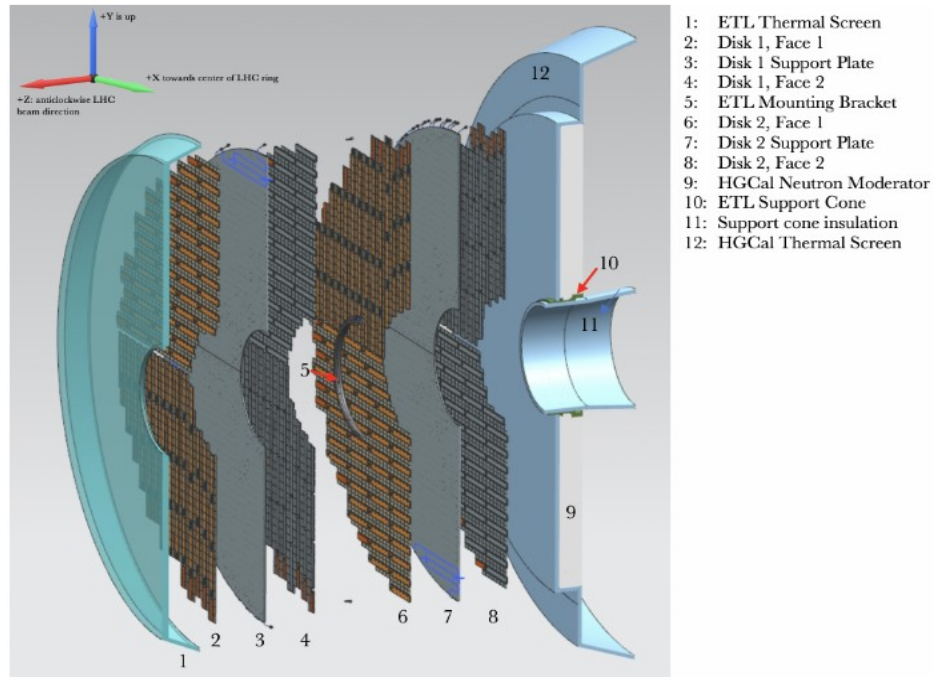


Figure 8. Representation of the ETL with its parts. Here it is easy to identify the two-disk system, supports, thermal and backward particle scattering (neutron moderator) protections as well as the detectors disk active regions (gray zones) and the support cone [16].

1.3. Energy loss and particle detection

As a particle travels through matter, it interacts with its constituents losing energy through different kinds of interactions. A charged particle can excite the electrons, interact with the nuclei, ionize atoms, participate in chemical and nuclear reactions and even pass its energy to molecule oscillations in the lattice. The mean energy loss per length unit can be expressed by the stopping theories of Bohr, Bethe and Bloch (4-5).

The 1913 Bohr theory was not designed, in principle, for the same scenario that the Bethe-Bloch theory. Due to the postulation time its approach did not take into account the quantum mechanical nature of particles and was useful only for very specific values of charge and speed that are not fully contained inside the practical range of the Bethe's theory from 1930 [20]. Both theories are based in the fixed energy values that usually materials present for the excitation of an electron and the ionization of its original atom. As these values are constant for each different material, the total number of ionizations after

the particle has crossed the medium is proportional to the energy it lost while moving through it, in other words, to the stopping power of the material (2) or the mass stopping power of the material (3) in case the densities ρ of the considered substances vary significantly or they are in different phases (the atomic number of the targeted substance Z is then relevant and thus considered in the electronic mass stopping formula as well).

$$S = \frac{dE}{dx} \quad (2)$$

$$S = \frac{1}{\rho Z} \frac{dE}{dx} \quad (3)$$

The Bohr and Bethe theories give pretty good approximation values for the energy loss inside their range of action. Bohr's formula is based on the classical conservation laws of energy and momentum and it works for heavy particles. These particles must travel at relative speeds lower than $2Z\alpha$ and much higher than α where Z is the atomic number of the charged particle, and α is the Sommerfield constant. On the other hand, Bethe's stopping theory approaches the issue using quantum mechanics to characterize light particle phenomena present when the particle interacts with the medium it is flying through

and it is valid when the relative speed of the particle is much higher than $\frac{1}{c} \sqrt{\frac{I}{2m_e}}$, where I is the mean excitation potential (if we consider electrons as classical oscillators then I is equal to $\hbar\omega_0$), m_e is the electron effective mass and c is the speed of light.

Different kinds of radiation interact through several mechanisms and at different depths in the material [21]. The electrons and heavy charged particles such as ions or protons lose energy mainly through momentum transference via Coulomb interactions with the electrons present in the material. They can lose energy by scattering with nuclei, and participate as well in nuclear reactions. Besides, based on the speed and mass of the particle it can lose high amounts of energy through Bremsstrahlung. Neutrons and photons have no charge and thus present no Coulomb interaction while moving through a detector. It is only after interacting with nuclei that they partially or totally transfer their energy to the material, but it is also probable that this does not happen and the particle leaves the medium without affecting it at all. Neutral particles scatter elastically, inelastically and

participate in nuclear reactions, while photon energy can be lost via photoeffect, pair production and photonic nuclear reactions.

When studying the electronic stopping of charged particles (except for electrons), due to the large number of collisions and the various changes that the potential of the charged particle can suffer during its way through the material, the calculations for the total energy loss are limited to approximations based on the average from all the events happening and the different assumed charge states while these events occur. This way, after integrating for all the impact parameters, the Bethe formula for energy loss would look like it is shown in (5).

$$-\frac{dE}{dx} = \frac{e^4 z^2 N_A Z \rho}{4 \pi \epsilon_0^2 m_e v^2 A M_u} \left[\ln \frac{2 m_e v^2}{I (1 - \beta^2)} - \beta^2 \right] \quad (5)$$

Here, z is the charge measured in electron charges, N_A is Avogadro's number, e is the electron charge, ϵ_0 is the vacuum permittivity, m_e is the electron effective mass, A is the relative atomic mass of the medium (in our case silicon) and M_u the material molar mass constant. β is the relative speed of the particle that can be neglected in non-relativistic scenarios.

The Bloch correction to the Bethe's formula helped to build the bridge between low and high speed particle cases, making use of the distant and close classification that both Bohr and Bethe theories share to cover their main flaws: the classical scattering generalization of the Bohr's model that dramatically reduces its range of action, and the omission of non-linear terms of the Bethe formula in free Coulomb scattering. Bloch correction to Bethe's formula is valid for most charged particles traveling through a material (6) [22].

$$-\frac{dE}{dx} = \frac{e^4 z^2 N_A Z \rho}{4 \pi \epsilon_0^2 m_e v^2 A M_u} \left[\ln \frac{2 m_e v^2 E_{kmax}}{I (1 - \beta^2)} - 2\beta^2 - \delta - 2 \frac{C}{Z} \right] \quad (6)$$

The correction introduces E_{kmax} - the maximum kinetic energy transferred in a single collision, δ - the density correction and C - the shell correction that makes the formula correct as electrons are not stationary inside the material.

In the case that the charged particles happened to be electrons, the scattering happens more frequently and the Bethe-Bloch formula requires the next modification [23]:

$$-\left(\frac{dE}{dx}\right)_{Coulomb} = \left(\frac{e^2}{4\pi\epsilon_0}\right)^2 \frac{2\pi z^2 N_A Z \rho}{m_e c^2 \beta^2 A} \left[\ln \frac{E_k \beta^2 (E_k + 2m_e c^2)^2}{2I^2 m c^2} + (1 - \beta^2) - (2\sqrt{1 - \beta^2} - 1 + \beta^2) \ln 2 + \frac{1}{8}(1 - \sqrt{1 - \beta^2})^2 \right] \quad (7)$$

The losses by Bremsstrahlung in the generation of X-rays (Figure 9) from the deceleration of the charged particle in the electric field of nuclei are significant at high electron energies or in heavy material mediums. Due to the lower mass of electrons they lose energy from this effect at a rate of approximately 10^{13} times higher than protons, thus their total energy loss needs to include an extra term for it [24]:

$$\frac{dE}{dx} = \left(\frac{dE}{dx}\right)_{Coulomb} + \left(\frac{dE}{dx}\right)_{Bremsstrahlung} \quad (8)$$

$$-\left(\frac{dE}{dx}\right)_{Bremsstrahlung} = \left(\frac{e^2}{4\pi\epsilon_0}\right)^2 \frac{Z^2 N_A (E_k + m_e c^2) \rho}{137 m_e^2 c^4 A} \left[4 \ln \frac{2(m_e c^2 + E_k)}{m c^2} - \frac{4}{3} \right] \quad (9)$$

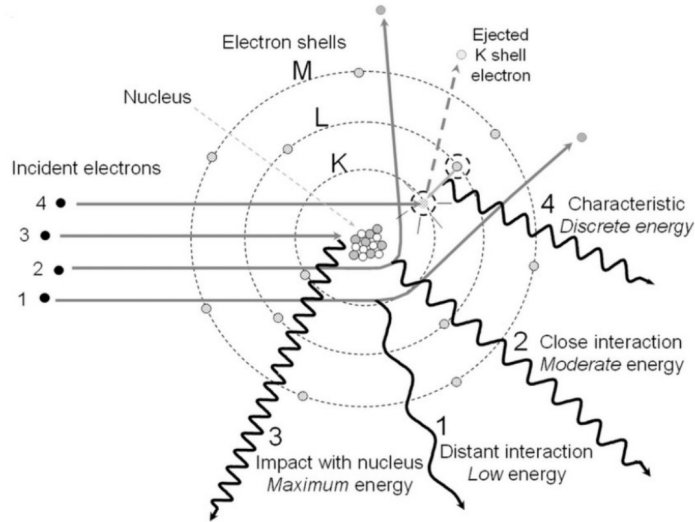


Figure 9. Bremsstrahlung energy loss mechanism for electrons [21].

Energy loss through scattering describes Landau's distribution with the presence of a longer tail as shown in Figure 10, due to the secondary scattering ionization generated by material excited electrons with high enough energy to ionize other atoms.

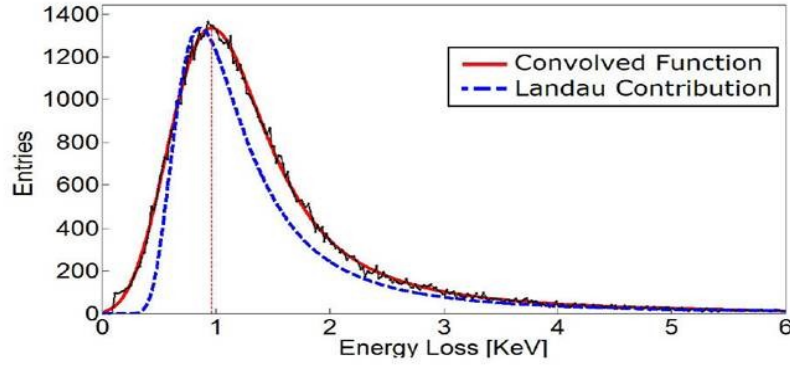


Figure 10. Example of scattering energy loss from protons traveling through a material with a long δ -tail for secondary ionizations.[24]

The part of the energy lost by the particles that ionizes the material generates carriers that can be directed using a voltage source and interpreted as a signal from a detector. The energy they carry after the collision in the accelerator falls into the Bethe-Bloch theory energy interval. From the interactions with nuclei, energy is added to the oscillations of the lattice translating into heat.

Even though Bethe's model with shell, Bloch and Barkas[25] corrections has been accepted as the standard after the creation of the first heavy-ion collider around 1950, there are still researches going around aiming for the reinserction of Bohrs theory to modern radiation physics problems for non-relativistic particles, some examples are available in [20] and [26].

The complete picture of the energy loss dependence on the particle energy is exemplified in figure 11, it is divided in several regions and explained by different models that reveal the value of the MIP. This value corresponds to the minimum expected response of the material to a particle traveling through it and defines the sensitivity parameter in the designs of a detector.

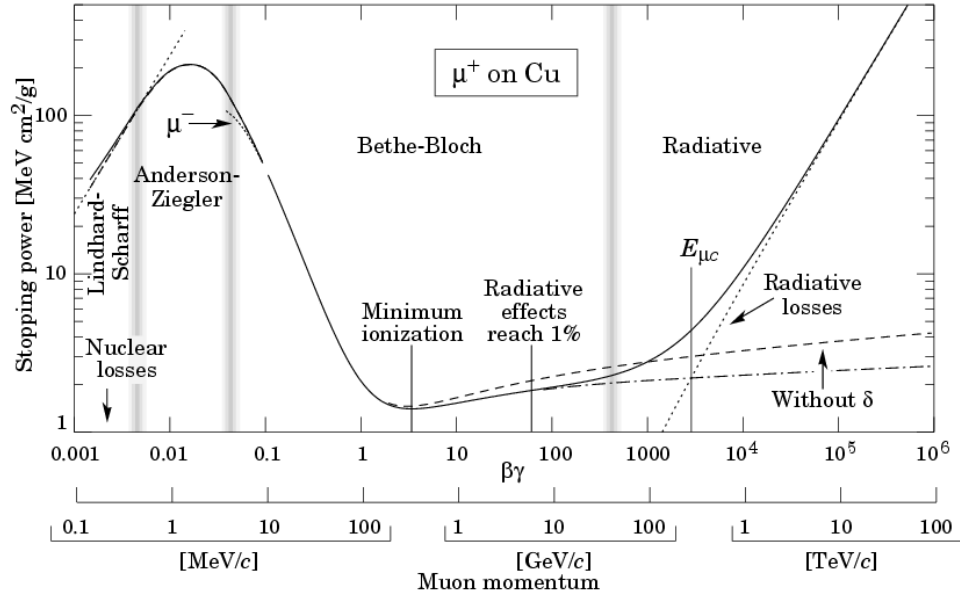


Figure 11. Energy loss for positive muons in copper [27].

In an average sized detector, a charged particle traveling through the body of the device can generate up to $2 \times 10^4 \text{ cm}^{-3}$ electron-hole pairs [15]. This amount is minimal compared with the carrier concentration already existing in the bulk. Non-doped silicon crystals have an average carrier concentration of 10^{10} cm^{-3} thermally generated at room temperature as the processes of spontaneous generation and recombination of carriers inside the crystal are in equilibrium while not being stimulated by any external source.

In order to measure the signal generated only by the traversing particle the amount of carriers in the crystal must be reduced drastically. Refrigerating the detector till the amount of carriers is reduced enough is not only suboptimal but expensive, therefore the detector must be fully depleted by applying reverse bias voltage to the pn-junction. This way, the bulk of the detector is cleared from any carrier that is not consequence of the pass of a charged particle through the device. The generated electron-hole pairs will travel to their respective electrodes where the read-out electronics will record and transmit the signal to be stored.

1.4. Silicon detectors

Semiconductors have caught the attention of researchers on detector design for applications in fields such as high energy physics, particle physics or even aerospace engineering since the middle of the last century. Their main advantage over other kinds of

detectors is a lower energy value of the MIP required to generate a strong signal over the level of noise.

Silicon is a very common material on earth and a common material for semiconductor detectors. Its crystalline form is very stable and it can be operated at room temperature. Silicon presents an indirect band gap of 1.12 eV at room temperature, which is significantly higher than the thermal energy at 300 K (25.9 meV approximately). When a particle travels through the bulk of an intrinsic silicon detector it ionizes the atoms of the lattice, generating electron-hole pairs. The energy required for such generation is 3.6 eV, which is much less than the ionizing energy required by gas based detectors (around 30 eV), meaning that a single particle traversing the bulk triggers the generation of approximately 80 to 108 e-h/ μm in silicon, which is 10 times more carriers than the ones generated in its gas-based counterparts [15].

Modern fabrication methods like floating-zone or magnetic Czochralski method allow the production of monocrystalline intrinsic silicon (CzSi) of high-purity with desired amounts of light impurities to enhance some beneficial properties like nitrogen[28], which increases the mechanical strength of the wafer, or oxygen, which improves the radiation hardness of the crystal[29].

The improvement in the energy resolution of semiconductor based detectors allows the fabrication of very thin devices, between 500 and 100 μm and even 45 μm . These will be discussed further in this work. While developing new detectors for high energy experiments such as the CMS experiment the fundamental characteristics to take into account are a good energy resolution, high granularity, fast enough time response to solve bunch crossings, efficient pattern recognition and reconstruction and, one of the most important aspects to improve, radiation hardness [10].

1.4.1 Structure

The silicon-based detector structure of our interest is the one of a modified avalanche photodiode in between two ohmic contacts with a highly doped thin implant and a low doped bulk several times thicker where the detected signal is expected to be generated (Figure 12).

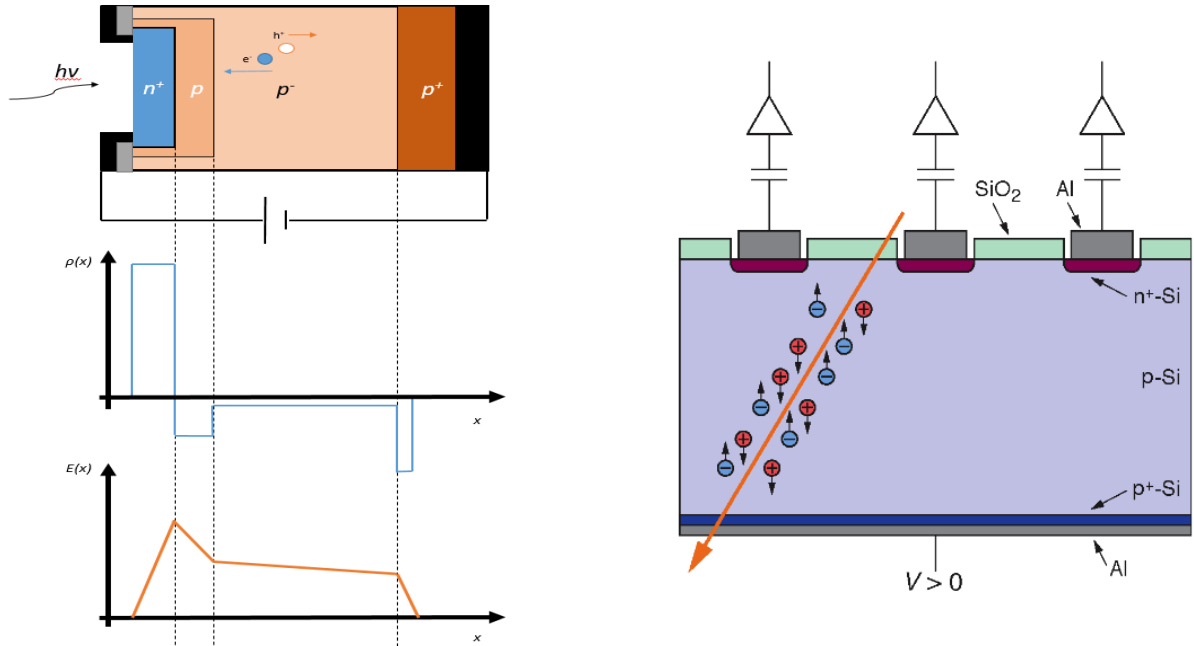


Figure 12. On the left, structure of an avalanche photodiode with SCR and electric field distribution along the sensor. On the right, the basic scheme of a silicon n-in-p particle detector [30].

1.5. Pn-junction

In a semiconductor, free carriers can flow via two mechanisms: diffusion and drift. Carriers participating to diffusion tend to displace from sites of high concentration to sites of lower concentration. Diffusion of carriers occurs proportionally to the delta of concentration in the device. This proportional diffusion coefficient is defined by the Einstein's relation (10) [31]:

$$D_{h,e} = \frac{\mu_{h,e} K_b T}{q} \quad (10)$$

Where q is the carrier charge, $\mu_{h,e}$ is the carrier (holes or electrons respectively) mobility, K_b is the Boltzmann constant and T is the temperature.

On the other hand, the carrier drift is the displacement caused by an external electric field that can be generated by stimuli of different nature such as light or an applied bias voltage. Carriers under constant electric fields acquire constant velocities when traveling through the semiconductor. As the carriers are charged particles, their flux generate a current

directly proportional to the magnitude of the electric field in the direction of the movement. The intensity of this current then is only limited by the carrier availability in the device and the mobility these carriers in that specific material.

When adding the values of these currents we can calculate the carriers' total current density in the device. As the carrier density can vary not only along the device, but during different moments in time as well, the carrier concentration and its gradient can be functions of time if the system is not static but dynamic:

$$J_{h,e}(x,t) = q\mu_{h,e}n(x,t)E(x,t) \mp qD_{h,e} \frac{\partial n(x,t)}{\partial x} \quad (11)$$

The pn-junction in a silicon detector collects the generated charges that drift towards their respective electrodes [15]. There is a difference in the electrostatic potential in both sides of the junction due to the high concentration of impurities of different nature (acceptors for the p-type and donors for the n-type). This difference shows up as an energy barrier that low energy carriers cannot cross increasing the resistance of the device and adding a capacitance whose value is defined directly by the electric field in the junction [31].

As the carriers start to diffuse from the side of the junction with higher concentration to the lower, the lattice atoms start to ionize. At room temperature it is expected that the totality of the impurity atoms is ionized together with a small portion of the intrinsic atoms as well. This ionization creates an electric field with the opposite sign in the nearest zones of the junction called the space charge region (SCR) (Figure 13). At this point the flux of carriers is stopped almost completely between n- and p- silicon as the electric field from the opposite side of the junction is strong enough to stop the carriers from crossing. The size of this region is defined by the potential in the junction, thus it decreases with a higher impurity concentration.

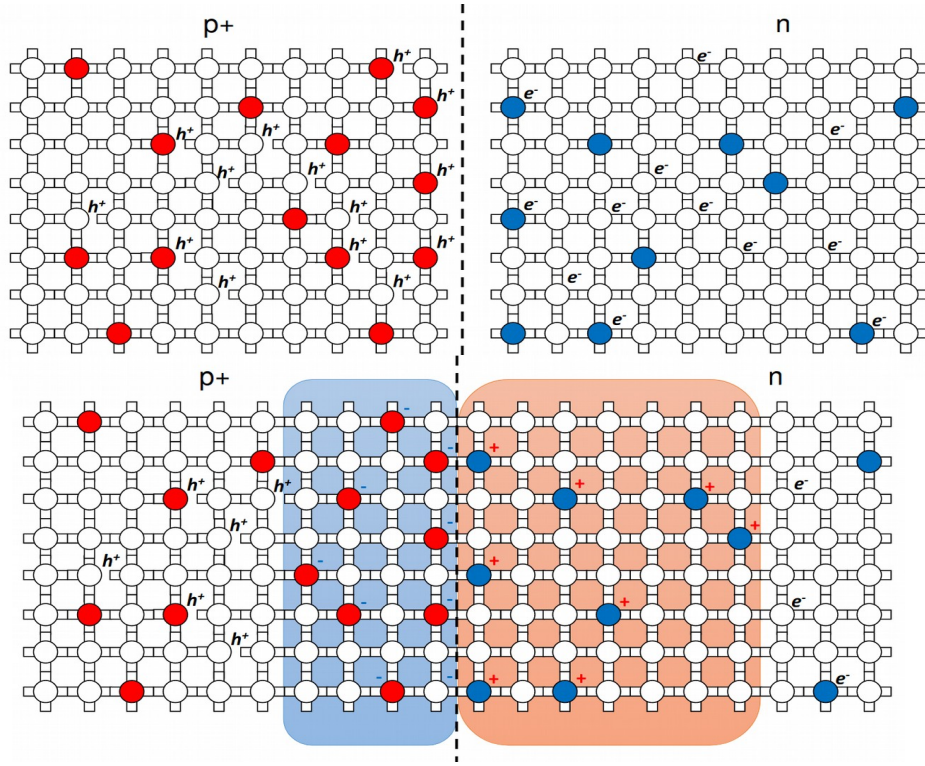


Figure 13. Up, room temperature (fully ionized dopant) representation of two separated silicon lattices with different grade and type of doping, silicon atoms are in white, donors in blue and acceptors in red. Down, a pn-junction is formed. Carriers diffuse through the junction till the SCR is formed. The SCR is indicated by the colored rectangles.

As the charge density in the SCR is no longer zero, the electric field in the junction can be obtained by:

$$\epsilon E_x(x) = \int \rho(x) dx \quad (12)$$

Therefore, according to the Poisson's equation for the electrostatic potential, the potential in the junction is described by a second order differential equation with one unknown:

$$E_x(x) = \frac{-\partial \phi(x)}{\partial x} \Rightarrow \phi(x) = - \int E_x(x) dx \quad (13)$$

$$\frac{\partial^2 \phi(x)}{\partial x^2} = \frac{-\rho(x)}{\epsilon} = \frac{-q}{\epsilon} \left[n_i \left(e^{\frac{-q\phi(x)}{K_b T}} - e^{\frac{q\phi(x)}{K_b T}} \right) + N_d(x) - N_a(x) \right] \quad (14)$$

In an abrupt pn-junction, such as the one we are looking at in this work the charge density function is predictable along the semiconductor and can be approximated through

iterated integration methods. The band theory together with the calculated potential allow us to construct an energy diagram for the pn-junction (fig 14.):

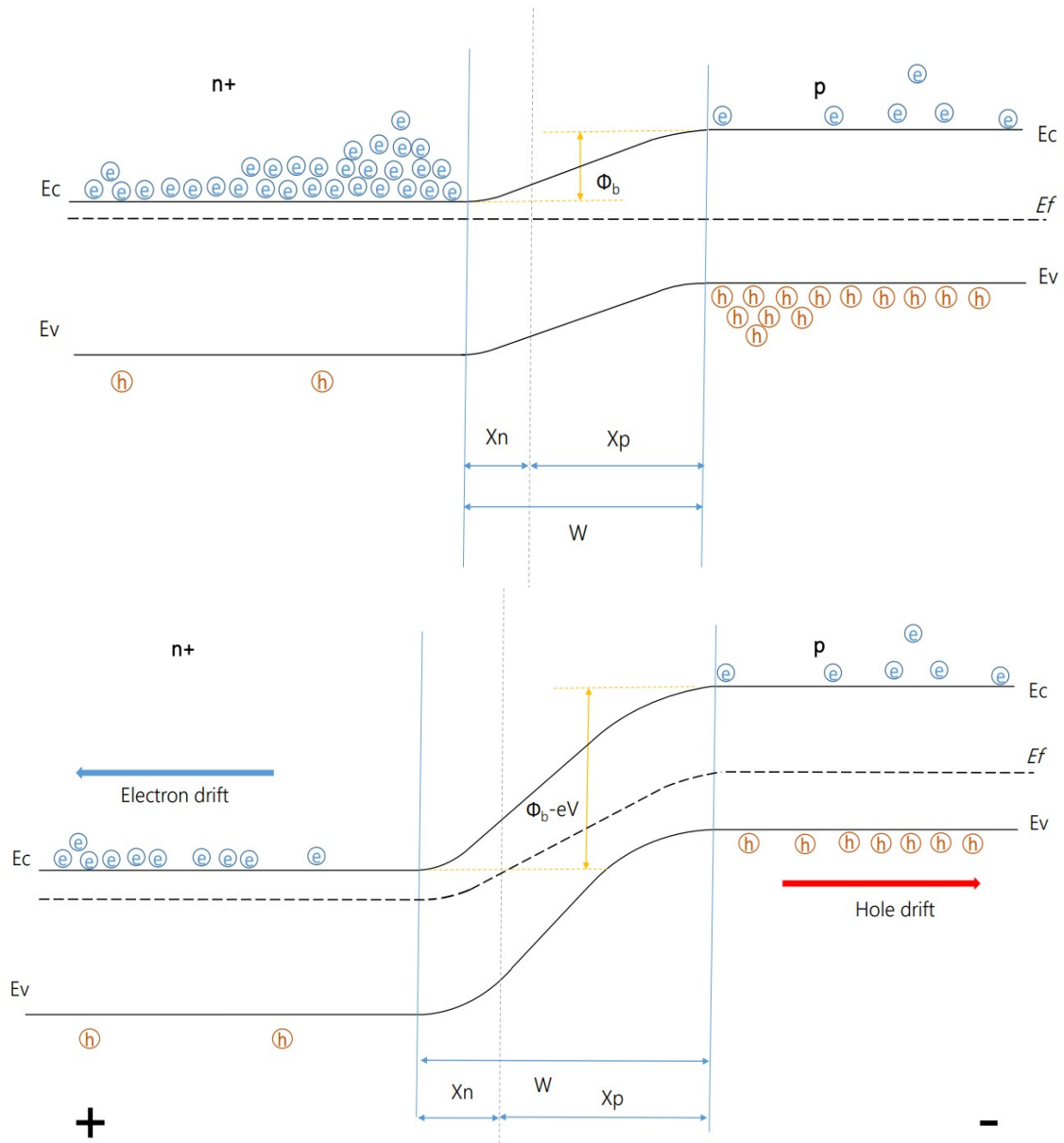


Figure 14. Representation of the energy diagram of a pn-junction, this time with a highly doped n-type semiconductor. The difference of electrostatic potential between both sides creates a barrier for carriers that corresponds to the electric field of the SCR.

The total size of the SCR can be approximated by solving the potential equation using boundary conditions: in the junction at $x=0$, where the electric field and the

potentials from both sides are supposed to be equal at equilibrium state, and in the place where the potentials become constant (x_n, x_p). Solving the potential equation taking into account the decrement in the potential gap due to the presence of the opposite charged ions at the other side of the junction, shows the local SCR size dependence on the neighbor semiconductor impurity concentration (7). The total size of the SCR is then obtained by simply adding the values of the local SCR from each side of the junction. The potential ϕ at (7) and (8) defines the size of the depleted region as well, that is why any external voltage applied to the junction will change this potential and thus the depletion region size:

$$x_p = \sqrt{\frac{2 \epsilon \phi}{q} \frac{N_{Dn}}{N_{Ap}(N_{Ap} + N_{Dn})}}, x_n = \sqrt{\frac{2 \epsilon \phi}{q} \frac{N_{Ap}}{N_{Dn}(N_{Ap} + N_{Dn})}} \quad (15)$$

$$w = x_p + x_n = \sqrt{\frac{2 \epsilon \phi}{q} \frac{(N_{Ap} + N_{Dn})}{N_{Ap} N_{Dn}}} \quad (16)$$

This way, we can modify the size of the depletion zone by changing the bias voltage. We can observe that the higher the dopant concentration the higher the value of accumulated charge near the junction, but also the higher the required voltage needed to change the width of the SCR.

Applying forward bias increases the amount of main charge carriers in the device, reducing the potential barrier height and thus the size of the SCR. On the contrary, if the bias is reversed, like represented in the Figure14, the carrier concentration near the junction starts to reduce gradually increasing the size of the depleted zone.

1.6. PIN diode

Photodiodes and silicon detectors use a pn-junction with very different doping levels on both sides. The highly doped size depends on the type of particle that the electronics are designed to register (electrons or holes).

The particle radiation induced into the device excites the carriers in the lattice generating an electron-hole signal. In order to avoid the instant recombination of this pair,

the energy absorption from the ionizing particle must occur in the depleted region of the pn-junction [32]. Traditional photodiodes have a limited depletion region as the whole detector bulk cannot be depleted by reverse bias voltages before reaching breakdown, thus they lose signal intensity. That is why an intrinsic semiconductor layer is added between the n- and p- regions to allow the full depletion of the sensor. This device is called a PIN diode (Figure 15).

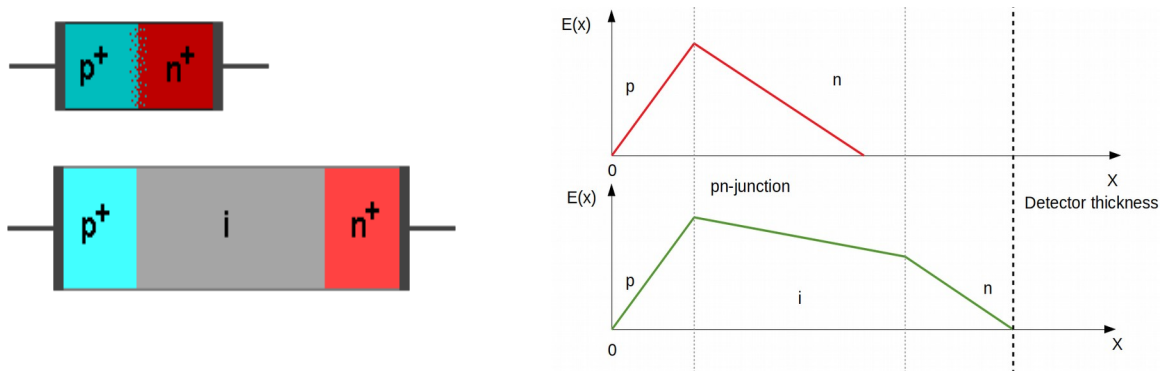


Figure 15. Electric field in a photodiode and in a PIN diode. The electric field that causes the electron-hole pairs to drift is present along the whole PIN diode after reaching full depletion.

Figure adapted from [33].

Thermal energy breaks the electron valence bonds and generates carriers in the lattice. As the signal generated in an average sized detector is composed by several tens of thousands of carriers and the average free carrier concentration in intrinsic silicon is of the order of 10^{10}cm^{-3} at room temperature, the device needs to be fully depleted for the signal to be detected by the readout electronics [34].

The full depletion voltage value needs to be significantly lower than the breakdown voltage of the detector, and it should be possible to fully deplete the detector during its full operation lifetime. The exact magnitude of the reverse bias changes as a consequence of the accumulated radiation. It can reduce the donor/acceptor density in the device, damage the lattice structure and create carrier trapping defects [35], modifying the effective dopant concentration and the potential inside the crystal.

1.7. LGAD

LGADs were developed in the last decade. Their working principle is the same of an avalanche photodiode with the particularity that the level of gain must be limited to a range around 10 to control the leakage current and to improve the S/N ratio for the charged particle detection. This can be achieved by modifying their doping levels to reduce the gain and the operational voltage of the device [36].

Avalanche photodiodes are used for γ -ray and X-ray detection via photon energy absorption. The signal generated is multiplied when the carriers go through a highly doped thin layer called “multiplication layer” that increases the potential difference at the pn-junction. In silicon, this sudden potential peak generates an electric field of around 300 kV/cm that fills the carriers with kinetic energy. The boundary crossing carriers then have enough energy to excite secondary carriers (typically electrons as they move faster than holes). This excitation is known as “impact ionization”, and can be triggered again by the secondary carriers as well, while traveling to the electrode, increasing this way the output intensity several times (Figure 16).

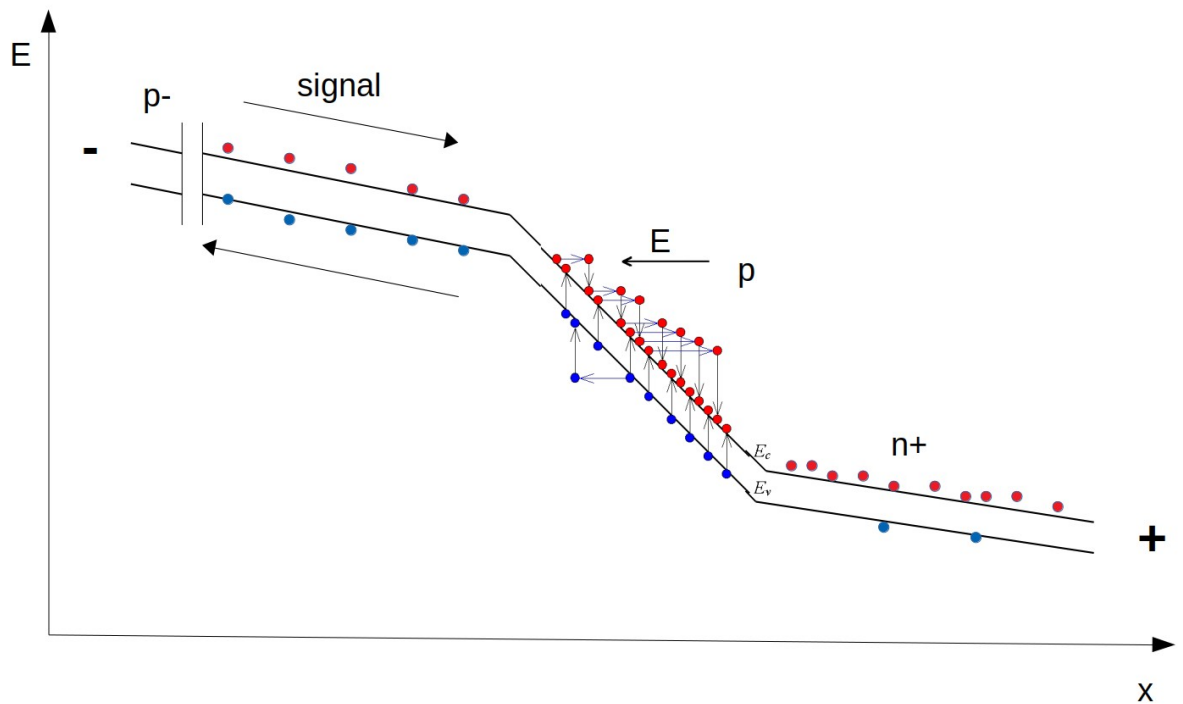


Figure 16. Energy diagram representation of the avalanche mechanism triggered by the impact ionization in an n-in-p detector. The electrons (red) are detected much faster as they have higher mobility than the holes (blue). One single electron can ionize several atoms during its passage through the multiplication layer. The holes' signal is also amplified by the multiplication layer but they are detected later as a transient signal. Adapted from [37].

The impact ionization phenomenon strongly depends on the electric field at the junction. It can only occur at high enough electric fields and it is defined by the ionization rate parameter of each kind of carrier (9) [38].

$$\alpha_{n,p} = \frac{E}{E_{th}} e^{\frac{-E_i}{E}} \quad (17)$$

Where E is the electric field in the junction, E_{th} is the minimum ionization energy at this high field (has different value for electrons and for holes) and E_i is the field threshold generated by ionization scattering.

The total free carrier generation by multiplication at the junction and at stable thermal conditions will be equal to:

$$G = \alpha_n n v_n + \alpha_p p v_p \quad (18)$$

Here, n and p are the free carrier concentration in the n and p sides of the junction respectively and v_n and v_p , the carrier drift velocity.

The most critical part of the LGADs is the multiplication layer. It must generate the correct value of gain and remain effective after irradiating the detector, and it must not influence negatively the breakdown voltage value. The signal gain is affected strongly by the doping profile of this layer, more specifically the effective doping profile (Q_{eff}) that expresses the average homogeneity of the impurity distribution in infinitely small traverse sections along the layer [36]. Naturally, a constant gain value along the whole detector bulk is expected for better position tracking. However, the edge field effects reduce the breakdown voltage of the device and break the isolation between nearby pads, making it necessary to find an equilibrium between homogeneous gain uniformity and edge field effect reduction.

Simulations carried out for silicon LGADs with breakdown voltages of 400 V and 500 V [36, 39] have shown that the minimum Q_{eff} value required for a gain of 1.1 is

around $1.6 \times 10^{12} \text{ cm}^{-2}$ [36]. This value is known as Q_{eff}^{crit} or critical effective doping profile.

The same researches have also showed that a dopant concentration from 4 to 5 $\times 10^{16} \text{ cm}^{-3}$ for the multiplication layer (for n-in-p detectors) is the ideal one to achieve gain values between 5 and 15 at over-depletion voltages, and that increasing the dopant concentration in the bulk strongly increases the breakdown voltage.

The LGADs were born as a solution for the problem of detectors' low charge collection after irradiation inside high energy physics experiments. However it has been observed that LGADs often loose their gain after irradiation and behave like common PIN diodes [36]. Nevertheless, experimentation shows that by reducing the thickness of the active region a more radiation resistant detector would be obtained in exchange of some charge collection in the non-irradiated state. This property of the LGADs is very promising for the development of timing detectors, as the gain in thin LGADs can be maintained at the same level than in thicker detectors with less bias voltage and a pulse width of the transient currents much shorter which translates to a better time resolution (Figure 17). The devices that make use of this characteristic for timing detection are called ultra-fast silicon detectors (UFSD).

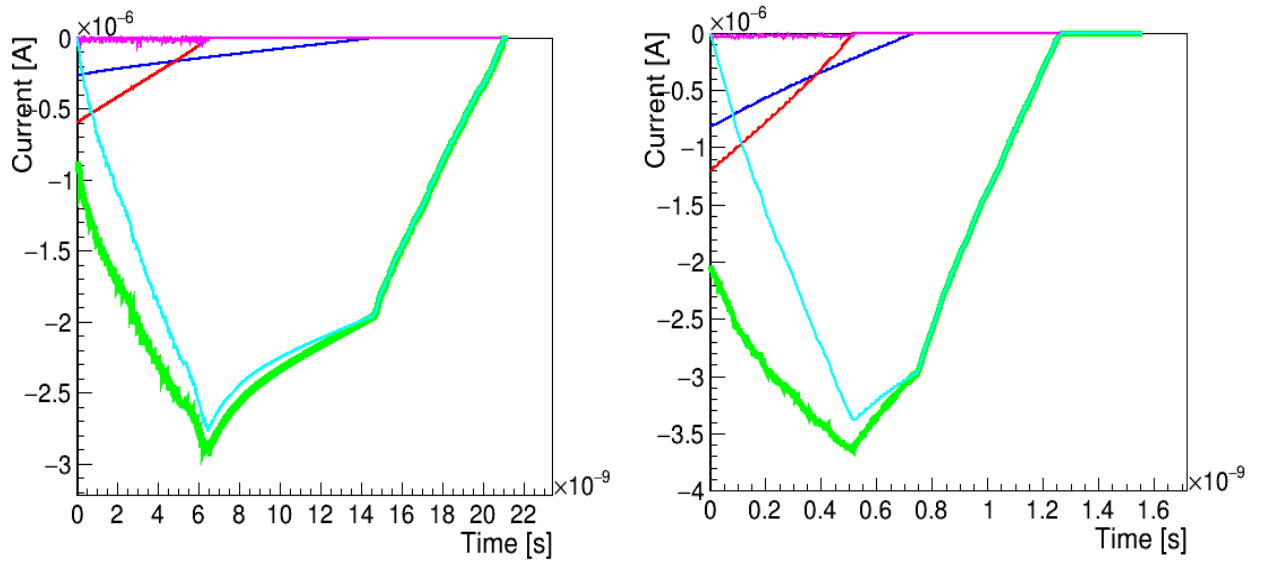


Figure 17. Weightfield 2 simulation of the signal pulse generated inside non-irradiated n-in-p LGADs of 300 μm (left) and 50 μm (right). The gain level in both detectors can be maintained while the pulse width ($I(t)$) is an order of magnitude lower for the thin LGAD.

These new technologically advanced sensors conceived at the “Centro Nacional de Microelectrónica” (CNM) in Barcelona, are being developed to solve future obstacles in high-energy physics experiments such as the ones at the LHC, now that they have reached high luminosity levels and the data from the collisions requires more precise separation of events. The UFSD gain value and short pulse widths are being tested before and after irradiation with the aim to untangle pileup events in collision experiments that hide crucial information about the existence of yet undiscovered particles. The challenge was to design detectors with enhanced time detecting capabilities, at the same time not to make them too large to lose the required spatial resolution.

The gain generated by an LGAD after irradiation significantly decreases compared to its initial state. The thicker detector usually suffers a higher diminution of signal as its higher volume makes it more susceptible to defect clusters, carrier trapping and impurity displacement compromising this way the quality of the signal even before it reaches the multiplication layer.

Originally the device design aimed towards a resolution of 10 μm for spatial coordinates and 10 ps for the timing of a particle event. The main parameter to have in mind for applying LGADs in timing detection is the slew-rate. It represents the detectors’ response time to a charged particle, the faster the voltage changes the better time resolution will the device have. However, factors such as high leakage current and radiation hardness requirements in ATLAS and CMS upgrades pushed the precision limits to 30 ps. This timing resolution is achievable by the joint work of four layers of sensors placed at the endcap for the CMS and at the front of the forward calorimeter for the ATLAS experiment [40].

The future of these low gain detectors is different depending on the requirements from the experiments in which they are going to be used. Electron colliders generate lower fluence values. They require cheaper materials and precise event positioning while muon/pion colliders’ main concern is the radiation hardness of the LGADs.

The objects of study in various researches to the present day are [41] the time resolution extension in fluence values over $2 \cdot 10^{15} \text{ n}_{\text{eq}}/\text{cm}^2$ (current limit) as colliders such as the Future Circular Collider (FCC) are planned to reach hadron collisions of around 100 TeV and a particle fluence of $10^{17} \text{ n}_{\text{eq}}/\text{cm}^2$ [42], the stability of the detectors at fluence

values over $10^{16} \text{ n}_{\text{eq}}/\text{cm}^2$ as the damage to the lattice at this irradiation level seems to be sufficient already to drastically reduce the gain and invert the bulk impurity type, killing the sensor, and the improvement of the positioning of the detector avoiding increasing the gain to levels where the S/N ratio would end up compromised.

1.7.1. Timing resolution

The timing resolution of an LGAD can be calculated using the formula [43]:

$$\sigma_t^2 = \sigma_{\text{timeWalk}}^2 + \sigma_{\text{LandauNoise}}^2 + \sigma_{\text{Distortion}}^2 + \sigma_{\text{jitter}}^2 + \sigma_{\text{TDC}}^2 \quad (19)$$

The basic terms of the time resolution core are the time walk, the jitter and the time-digital conversion (TDC) binning. The TDC term depends directly on the speed of the electronics, this dependence is usually expressed as an uncertainty [44]

$$\sigma_{\text{TDC}} = \frac{\text{TDC}_{\text{bin}}}{\sqrt{12}} \quad (20)$$

where TDC_{bin} can be assumed as 20ps, due to the high level performance reached by the continuous upgrading of the electronics speed.

The time walk (fig 18. left) term refers to the difference in time rise of different signals with different amplitudes, due to the physics of signal formation [45]. It can be expressed as a root mean square (RMS):

$$\sigma_{\text{timeWalk}} = \left[\frac{t_{\text{rise}} * V_{\text{th}}}{dV/dt} \right]_{\text{RMS}} \quad (21)$$

In this term, V_{th} is the signal threshold, dV/dt represents the speed with which the signal changes known as the slope rate. Landau fluctuations present, due to the non-uniform charge deposition inside the sensor contribute in some grade to this term, while the distortion term contributes to the jitter term, as it depends on the uniformity of the operating field itself.

Jitter (Figure 18 right) refers to the variation in the amplitude of the signal due to electronic noise. The better the S/N ratio, the better resolution obtained from this term:

$$\sigma_{\text{jitter}} = \left[\frac{N}{dV/dt} \right] \approx \frac{t_{\text{rise}}}{S/N} \quad (22)$$

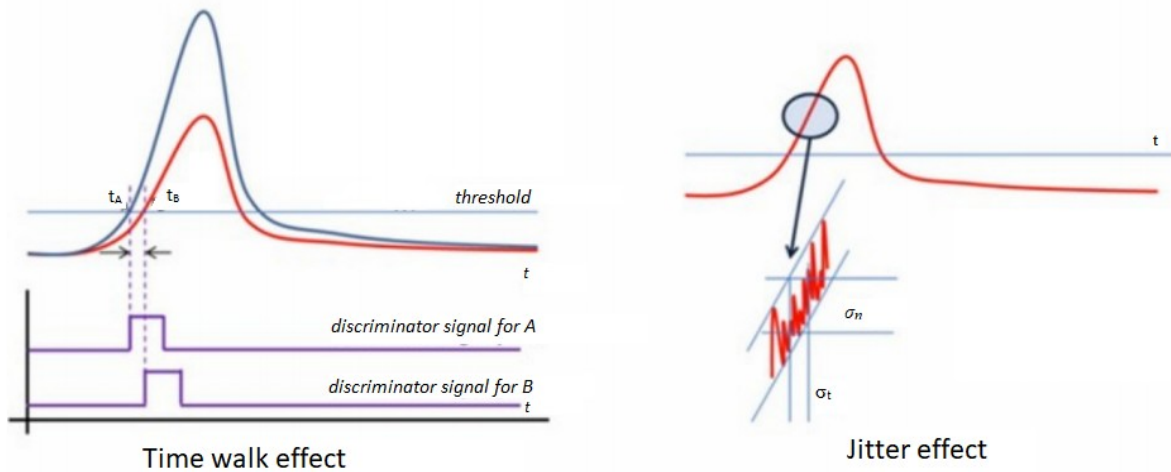


Figure 18. Representation of the time walk and jitter of a time signal [45].

Therefore, if the implemented electronics are the fastest available for the project, to have an outstanding time resolution the signals must be fast and present a high amplitude (through a high gain value). This can be achieved by using thin detectors with controlled level of gain [40]. Thin detectors reduce Landau fluctuations as well leaving only the noise factor to be minimized as much as possible. Experience also shows that thinner detectors present significantly lower rise times and lower bias voltages and require less power to obtain the same resolution [43].

1.8. Radiation damage

The defects generated by non-ionizing interactions are usually found inside the detector bulk. Due to collision the atoms can leave their place in the lattice and move forward to create a vacancy and interstitial defect, usually known as a Frenkel pair. The minimal energy needed for this event to happen is only 25 eV. While moving during this unwanted displacement, if the energy is around 5 keV, part of the energy ionizes atoms generating a large number of interactions that may cause clusters of defects and thus contribute to carrier trapping and efficiency reduction.

If we look closer to the surface of the detector, the distribution of defects is not uniform at all. The damage generated is due in its great majority to ionizing damage between the silicon oxide layer and the bulk and can bring changes to leakage current values [46].

As carriers may get trapped inside these defects, recombination and generation may occur easier there increasing the value of leakage current significantly. Decreasing the operative temperature has proven effective till some level controlling the leakage current generated by these defects. However, if carriers get trapped in the potential wells of the vacancies in the lattice a signal amplitude reduction can be observed directly proportional to the trap concentration, the thermal speed of the carriers and the trapping cross section [47].

The presence of secondary impurities such as oxygen or nitrogen has been proven not “harmful” for the capabilities of the detector but the opposite, and only the fluence and the temperature linearly affect the trapping probabilities of carriers decreasing by 20-30% at temperatures around -50 °C [48].

The reason why the preferred implant type is the n-type is due to the advantage that electrons have over holes in their mobility, clearing fast the volume of the detector leaving a signal consisting only of the transient current of holes. After investigating the radiation effects on different detector designs [15], it has been observed that irradiating the detector damages the lattice changing the amount of impurities in the bulk and, in our case, the reduction of impurities in the multiplication layer reduces the gain and produces a “conductivity type inversion” at some point, especially in n-type bulk detectors as vacancies can work as acceptors by trapping electrons in an intermediate state between the valence and the conduction level.

P-type bulk sensors are susceptible as well to this kind of phenomenon, but it presents itself later and milder than in the n-type ones. These are the main reasons why a pixel structure n⁺-on-p is the chosen one as the best candidate in high resolution, high radiation hardness and low signal detection delay for the UFSD.

2. EXPERIMENTAL METHODS

The samples measured in this work were part of the latest production of FBK UFSD3.2 and HPK HPK2 pad LGADs . The sensors were displayed in 2x2 arrays of 1.3 x.1.3 mm pads (Figure 19). Distinct types of 45 μm thick LGAD samples were measured with the aim to see the effects of different gain layer (GL) dopant dosage levels. For FBK samples performance changes due to the presence of carbon in the GL were studied as well (Table 1). Pads are protected from edge effects by guard rings and present optical apertures for the Transient Current Technique (TCT) measurements.

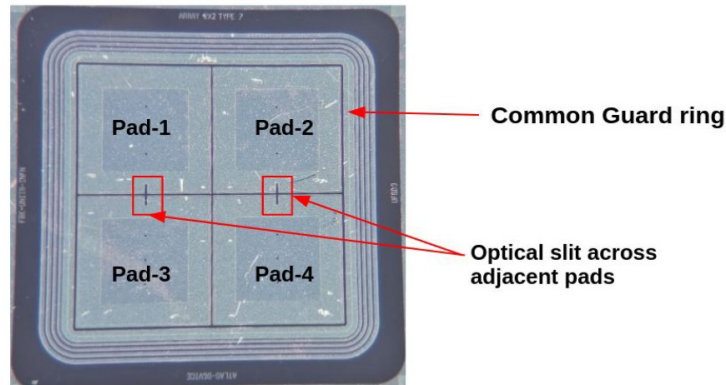


Figure 19. Photograph of a sample FBK sample and its parts.

Several studies are being carried out looking for ways of fabricating cheaper detectors maintaining the same or better performance that the actual LGADs. That is why samples were fabricated on magnetic Czochralski silicon wafers (the cheapest of the two modern high purity silicon production methods). The thickness of the samples is about 300 μm , but the LGADs active thickness is only 45 μm . The remaining silicon acts as an ohmic contact for the detector. FBK samples have also different interpad termination strategies (Table 1) with the objective of comparing the performance of different methods that may allow a reduction in the interpad gap size or may simplify the junction termination edge (JTE) creation process. Samples in this work were fabricated from three different wafers (W), W19, W13 and W10 and were produced with specifications corresponding to types presented on Table 1.

HPK samples are designed with different gain layer (GL) dopant concentrations to have different breakdown voltages (the higher the concentration the lower the breakdown voltage), being for number 28 160 V, for number 33 180 V, for number 37 220 V and for number 43 240 V.

Complementary annealing studies were carried out as well for proton and neutron irradiated samples to observe the degradation of the gain layer and the bulk full depletion voltages. HPK samples were neutron irradiated while FBK were proton irradiated at corresponding particle energies (Table 2). This way we were able not only to compare the performance before and after irradiation of each sample but also to make a comparison between the two manufacturers. Annealing times went from 60 minutes at 80°C up to values over 20000 minutes at the same temperature to observe how the efficiency of this method decreases exponentially with time for the radiation damage reduction in the samples.

Table 1. 2x2 UFSD3.2 samples specifications.

Type	Specification	Nominal width (μm)	Inter-pad design	strategy
1	L'(Dose Pgain) + 1*A (Carbon)+ Deep (GL depth)	16	Grid + extra grid	Aggressive
2	L'(Dose Pgain) + 0.6*A (Carbon)+ Deep (GL depth)	21	Grid	Medium
3	L'(Dose Pgain) + NIL (Carbon)+ Deep (GL depth)	21	Grid	Medium
4	M'(Dose Pgain) + 1*A (Carbon)+ Deep (GL depth)	24	Grid	Safe
5	M'(Dose Pgain) + 0.6*A (Carbon)+ Deep (GL depth)	25	Grid	Safe
6	M'(Dose Pgain) + 0.6*A (Carbon)+ Deep (GL depth)	28	Grid + extra grid	safe
7	M'(Dose Pgain) + NIL*A (Carbon)+ Deep (GL depth)	28	Grid + extra grid	safe
8	H'(Dose Pgain) + 1*A (Carbon)+ Deep (GL depth)	28	Grid + extra grid	safe

Type	Specification	Nominal width (μm)	Inter-pad design	strategy
9	H'(Dose Pgain) + 0.6*A (Carbon)+ Deep (GL depth)	38	2 p-stop	Super safe
10	L(Dose Pgain) + 1*A (Carbon)+ standard (GL depth)	49	2 p-stop + bias grid	Super safe
11	L(Dose Pgain) + 1*A-spray (Carbon)+ standard (GL depth)	21	Grid	Medium

Samples were irradiated with difference fluence values of protons and neutrons at energies included in the range of the MIP to test the sensitivity, resolution and radiation hardness of the LGAD pads. For protons, the average energy of the particles was 10 MeV and the fluence values were 1, 2.2, 3.87 and $6.5 \times 10^{14} \text{ p/cm}^2$. In the case of neutrons, the particle energy was 1 MeV and the fluence values included 4, 8, 15 and $25 \times 10^{14} \text{ n}_{\text{eq}}/\text{cm}^2$.

Table 2. Fluence correspondence of protons and neutrons irradiation.

#	Particle fluence for protons with mean energy of 10 MeV, $\times 10^{14} \text{ p/cm}^2$	Particle fluence for neutrons with mean energy of 1 MeV, $\times 10^{14} \text{ n}_{\text{eq}}/\text{cm}^2$
1	1	4
2	2.2	8
3	3.87	15
4	6.5	25

Finally, TCT measurements were carried out to calculate the fill factor after irradiation by measuring the interpad distances. The stability of the detectors operation at constant irradiation was measured in order to test their stability after irradiation as irradiated sensors are susceptible to “sparks” under prolonged operation.

2.1. CV-measurements

C-V Characterization is an important tool when studying the quality of detectors, as the device itself can be seen as a capacitor when fully depleted. Then, the voltage at which the capacitor gets fully charged corresponds to the full depletion voltage of the bulk, and the changes this value may experience after irradiation or operation define the severity of the lattice damage and contribute with the identification of new phenomena happening inside the detector like the presence of intrinsic spaces between highly doped layers, trapping centers generation or a change in the Q_{eff} value of the layers.

As the samples present gain layers, the C-V curves present two points of inflection corresponding to the full depletion voltages of the multiplication layer and the bulk. From these measurements, the real doping concentrations and the real doping peaks can be calculated.

Measurements were taken at the Helsinki Institute of Physics (HIP) Detector Laboratory's Karl Süss PM8 probestation (Figure 20). This set-up is displayed inside a dark enclosure or dark box that helps avoiding the excitation of the sample, due to photoeffect and undesired electromagnetic interactions. Under an optical microscope a vacuum pump keeps the sample in place on a chuck, while micrometric adjustable controllers allow the 3D displacement of tungsten probe-needles, similar to those used in scanning tunneling microscopy. Each probe is attached to an electrode that connects the sample with the electronics, which in turn consist of Agilent LCR meter HP-E4980A, Keithley 2410 source-meter and Keithley 6487 picoammeter. The control of the measurement parameters such as the voltage range or the frequency at the LCR meter is carried out using software created in MATLAB for the C-V measurements.

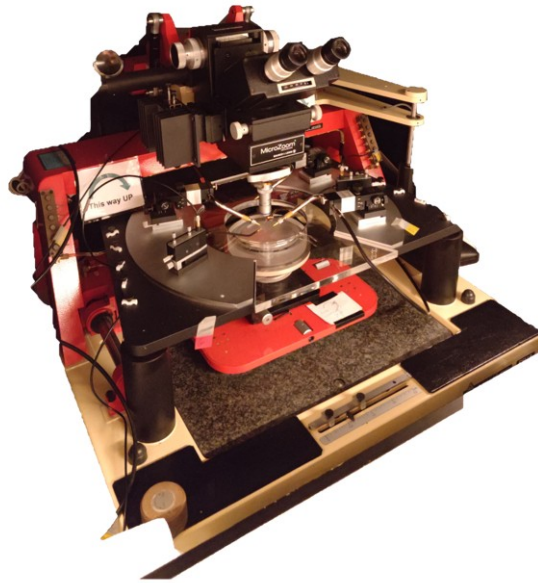


Figure 20. Probestation setup at HIP detector laboratory. Parts like the chuck, the probe-needles and the optical microscope are distinguishable in the image.

The characteristic capacitance measurement is carried out by the LCR meter. Probe-needles together with the chuck have the task of grounding and providing high bias voltage to the samples during the measurements. To protect the detectors' integrity, they were mounted on printed circuit board (PCB) prepreg and wire-bonded to copper foil on the same PCB (Figure 21).

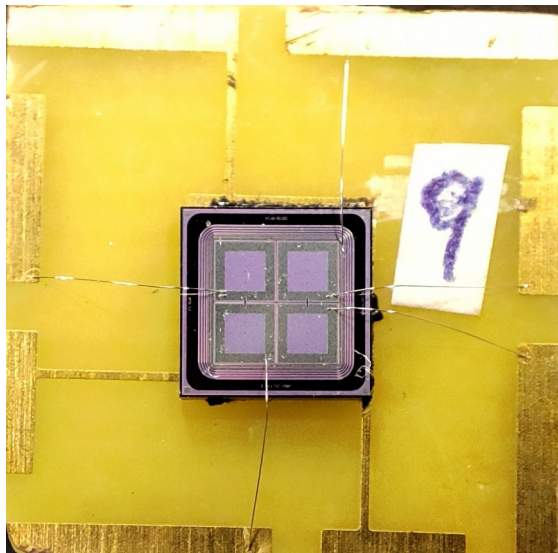


Figure 21. Samples' wire-bonding for probestation measurements.

This way, the chuck remained grounded as PCB prepeg is an isolator, the left micromanipulator supplied the high bias voltage to the copper patch connected to the back of the detector that would be the responsible for the detector's depletion, and the right micromanipulator recorded the sample signal as it is grounded through the LCR meter. It is worth mentioning that the "0 pads floating" method was implemented at the beginning by grounding all three pads that were not being measured with 3 complementary needles with their respective manipulators, this way isolating completely the objective pad. However, the observed results did not differ significantly from the simple 3-probe method (grounding to guard ring, high voltage to the back of the detector and measuring probe to the pad studied) reassuring the signal independence between pads. Thus, for simplicity and time saving purposes the 3-probe method was implemented for all the measurements.

Continuing with the capacitance - bias voltage curve construction, an AC signal is generated by the source-meter and then modulated by the LCR meter with a frequency of 1 KHz. Despite the source can reach values of 1 KV with a current of 1 mA, the LCR meter can work only for signals up to 1 V, but in exchange it offers an accuracy of 1 femtoFarad. To protect the LCR meter setup "safety boxes" and Isobox are used. The first ones protect the LCR meter's electronics from high voltages and unexpected tension peaks. Isobox is a complex circuit, designed to take the pulse signal received from the detector, send it to the LCR meter and filter it from the source high voltage to obtain amplitude and phase values generated only by the detector, while protecting the LCR meter from high voltage with the help of the safety boxes. The diagram of the complete setup is represented in figure 22.

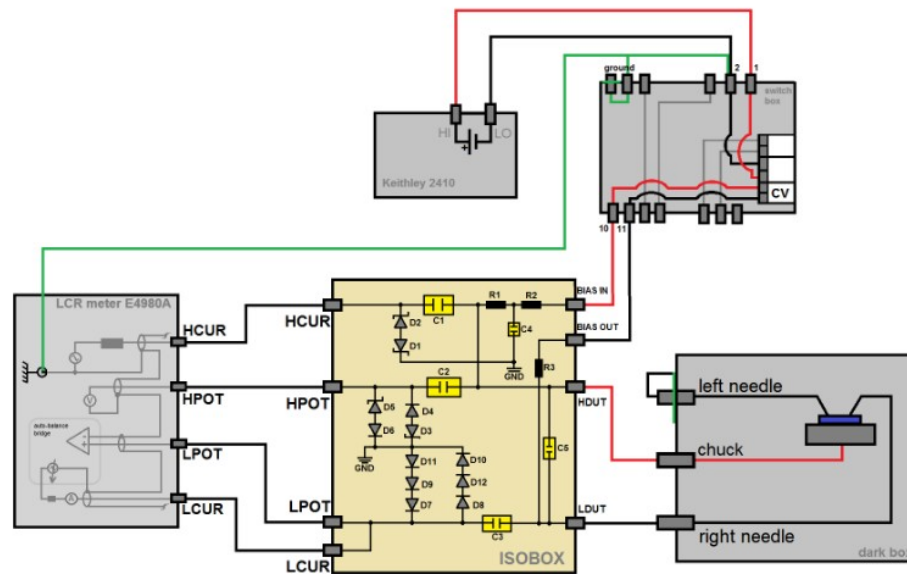


Figure 22. Diagram of the probestation C-V measurement setup.

2.2. Annealing studies

Annealing studies were carried out as a complementary analysis of the “self-regenerating” capabilities of detectors for different irradiation levels. Irradiated detectors were placed under a constant temperature of 80°C inside a Memmert oven type UE200 (Figure 23) during different periods of time. The time was exponentially increased to see until what extent this process would actually improve the characteristics of the detector.



Figure 23. Memmert annealing oven type UE200.

2.3. TCT-measurements

This technique consists of a 1064 nm infrared (IR) laser that works as radiation source for the emulation of particles crossing the detector. The detector then generates a signal that is captured and amplified by a wide band oscilloscope. The energy of the particle emulated is in the range of the MIP for silicon in order to characterize both the stability and the sensibility of the samples.

Due to the structure of the samples, the transient signal measured lasts only 2.5 ns for each particle crossing the 45 μ m thick LGAD (as the simulation in Figure 17 showed). The signal generated is composed mainly from holes that move from the gain layer through the bulk and towards to the p⁺ electrode on the back of the sample. Electrons are not only too fast but their signal decay pretty fast as they drift towards the n⁺ electrode through a shorter distance. Nevertheless, this peculiarity is linked only to this work as during operation in the actual experiment at the LHC it is expected to record the electrons as the signal carrying information from the LGADs.

The component parts of the TCT setup are: the IR laser, from which pulses were transmitted through an optical fiber to the focusing optics, the sample holder with 3D positioning micrometric controllers, a Keithley 2410 sourcemeter, a bias tee displacer for high voltage application to the sample, a wide band current amplifier and its correspondent Tenma power supply and an oscilloscope LeCroy WaveRunner 8404M-MS 4GHz. The whole setup is controlled by software created with LabVIEW on a PC.

3. RESULTS AND DISCUSSION.

The results of this work are presented in a comparative way. The first aspect evaluated and presented is the decay of the sensors' full depletion voltages of the bulk and the gain layers from the non-irradiated to the irradiated state. The results are presented in graphs separated by wafer number and detector type in figures from 24 to 30. The proton irradiated samples presented unstable and chaotic capacitance - voltage dependencies while the neutron irradiated ones were less unpredictable. Therefore, only several samples from this batch were candidates for further TCT analysis, which in turn is presented as a sequence of stability test, focus scan, voltage scan and finally interpad studies. Each one of these tests evaluated a different parameter explained in the discussion section, from figure 31 to 40.

Finally, annealing studies are presented as C-V curves for different annealing times showing what kind of effect an increment of the annealing time has in these samples and what can it be interpreted as.

3.1. Depletion voltage

The C-V curves consisted of 350 steps measured at 1 kHz, non-irradiated sample characteristics were added as a reference for detector degradation with radiation. In Figure 24 are presented the neutron irradiated FBK type 4 detectors and their respective non-irradiated reference detectors. The $1/C^2$ curves are presented to give a more clear understanding of the full capacitance value change of the samples with irradiation.

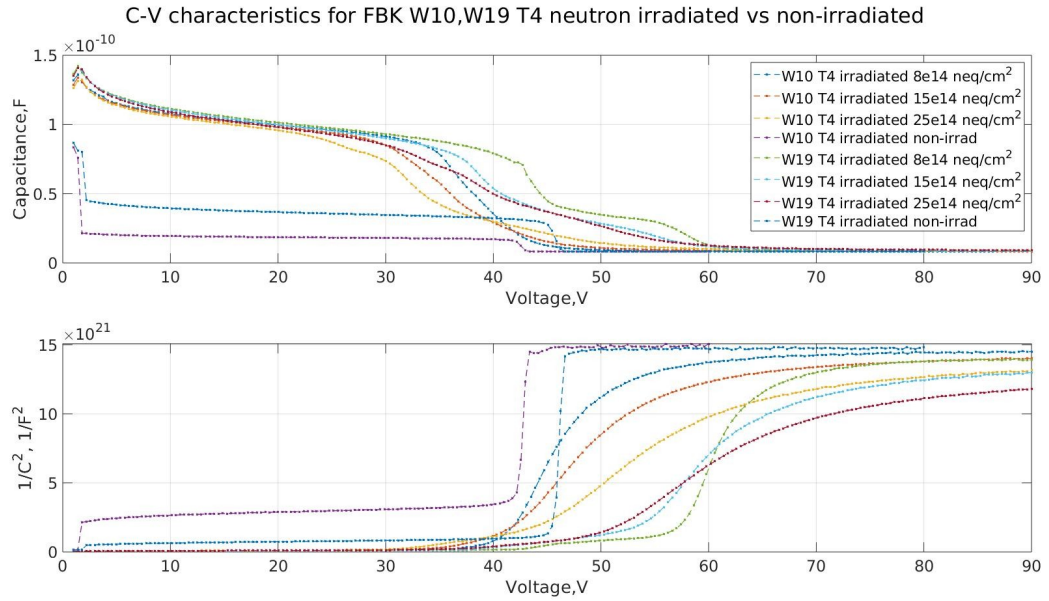


Figure 24. C-V and $1/C^2 - V$ characteristics for neutron irradiated FBK W10 and W19 detectors.

Figures 25 and 26 show the curves for the FBK proton irradiated samples. As it can be observed from the first sight, protons produce a more chaotic effect on the detectors. The damage can be so high that the LGAD starts behaving as a PIN diode.

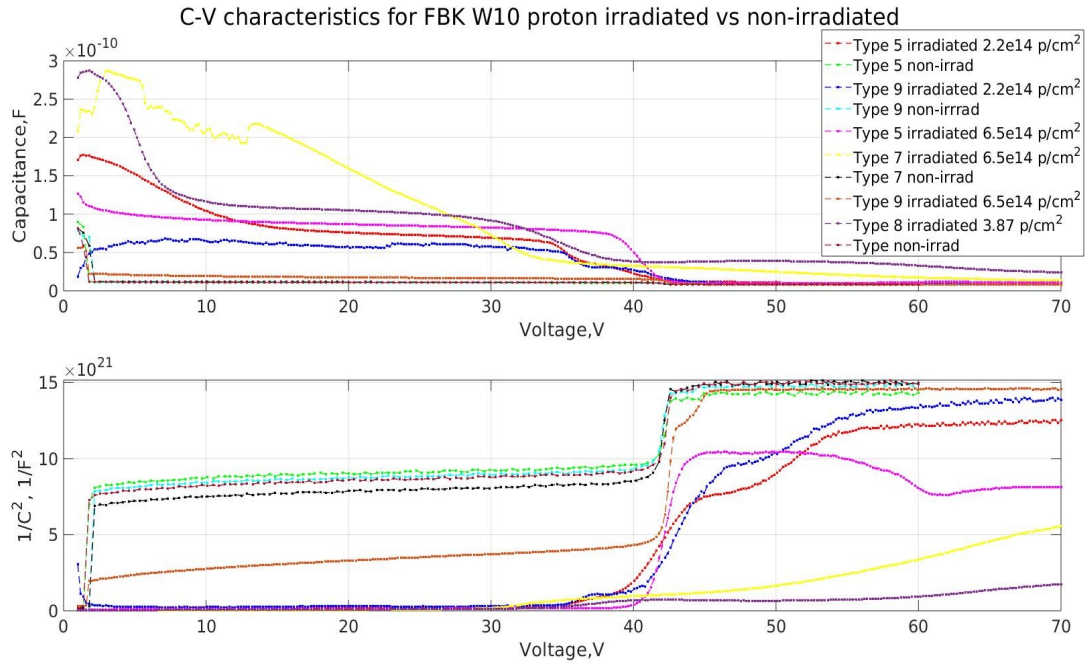
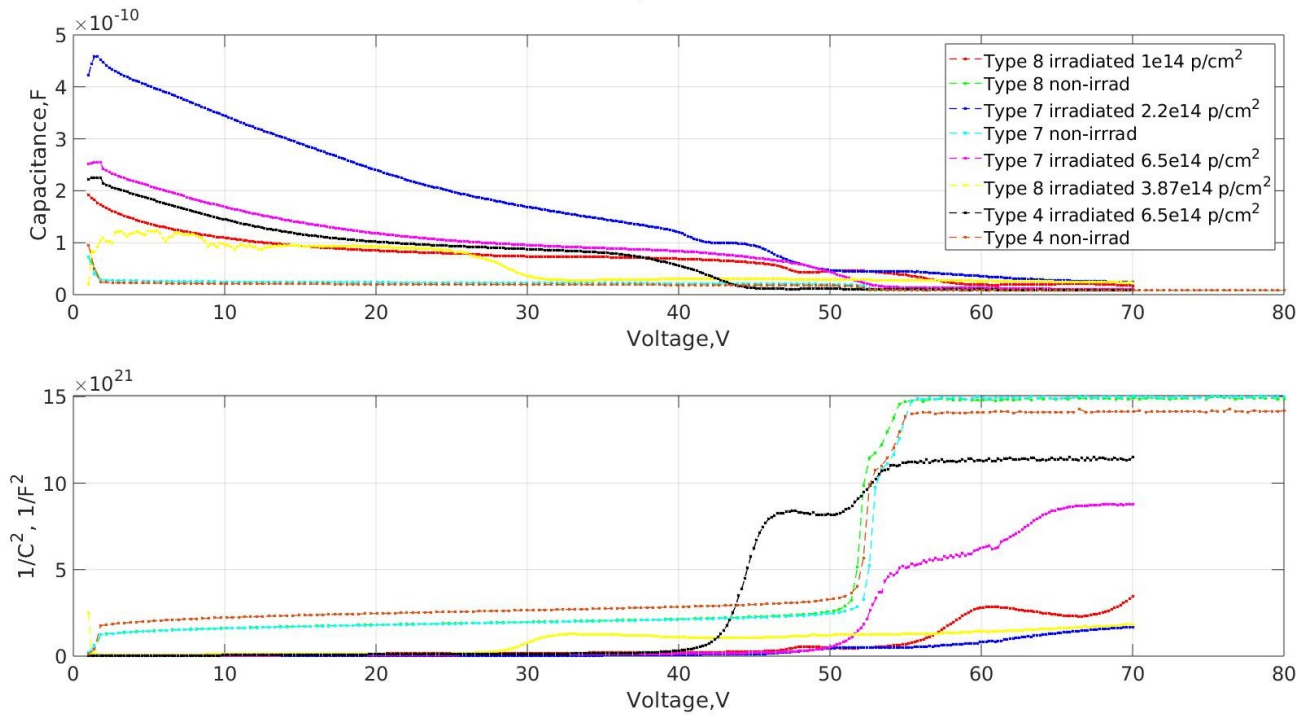


Figure 25. FBK W10 C-V and $1/C^2 - V$ characteristics for proton irradiates samples.

C-V characteristics for FBK W19 proton irradiated vs non-irradiated

Figure 26 . FBK W19 C-V and $1/C^2 - V$ characteristics for proton irradiated samples.

HPK samples were irradiated with protons as well, showing a more stable results.

The curves are reported in figures 27,28,29 and 30.

C-V characteristics for HPK W28 proton irradiated vs non-irradiated

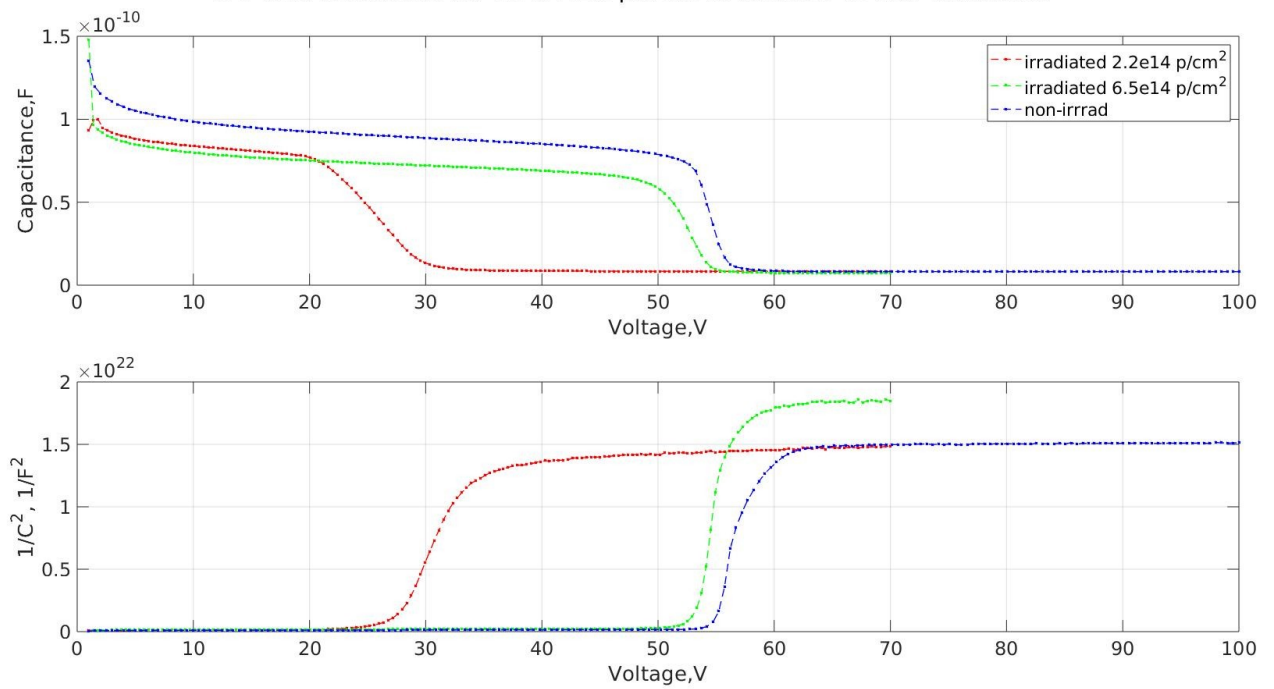
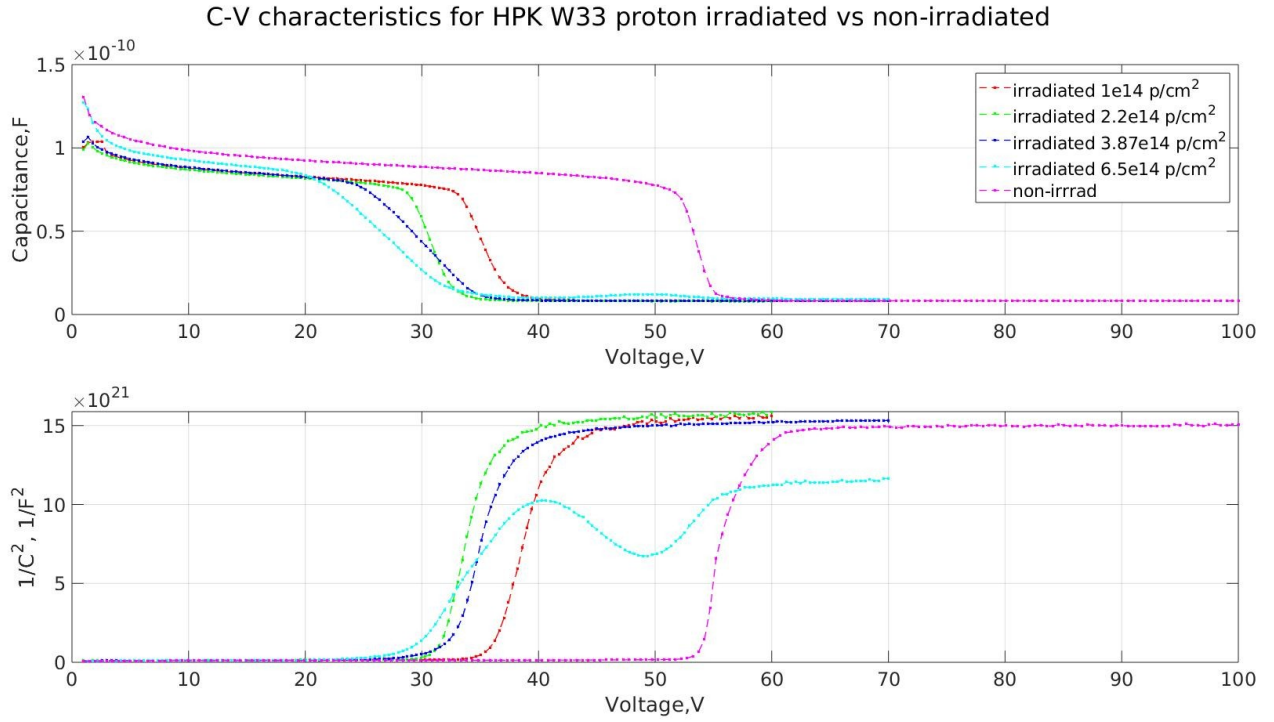
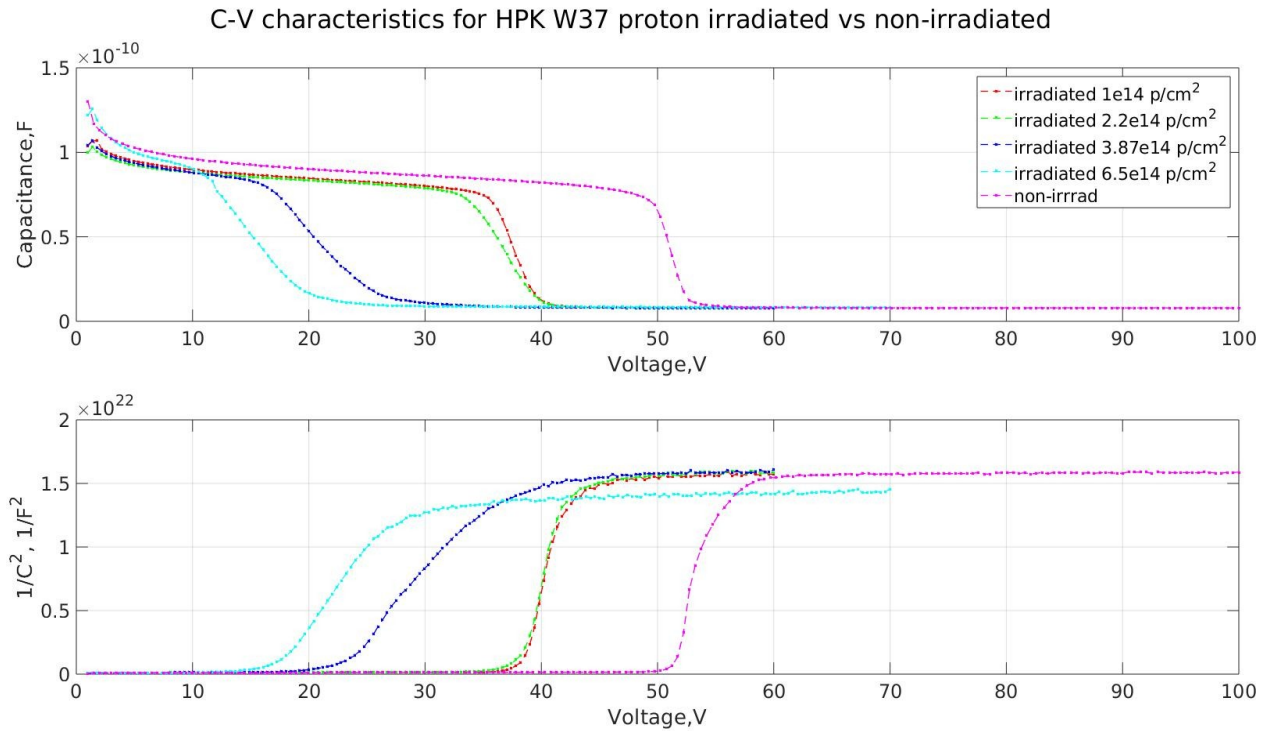


Figure 27. HPK W28 C-V and $1/C^2 - V$ characteristics for proton irradiated samplesFigure 28. HPK W33 C-V and $1/C^2 - V$ characteristics for proton irradiated samples.Figure 29. HPK W37 C-V and $1/C^2 - V$ characteristics for proton irradiated samples.

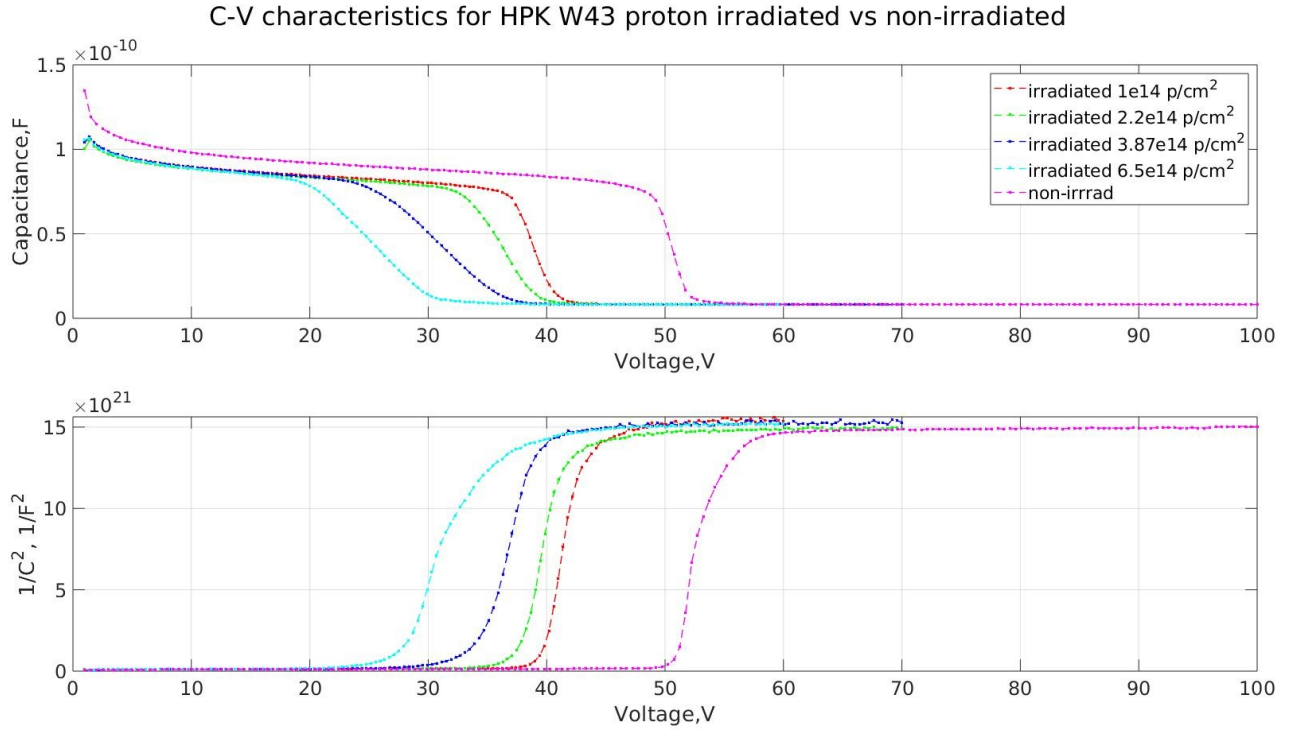


Figure 30. HPK W43 C-V and $1/C^2 - V$ characteristics for proton irradiated samples.

3.2. TCT measurements

The performance of irradiated samples was tested for 3 detectors with the TCT station. The nominal interpad distance values were expected to change as well as the values of the full depletion voltages. The rough scans presented in Figures 31, 35 and 38 allowed to locate the exact position of the optical apertures. As the intensity of the laser beam describes a Gaussian function along the optical axis of the measurements, the focus scans are carried out along the laser axis and one coordinate axis parallel to the sample surface to identify the exact spot coordinates where the detector generates the higher signal in response to the laser stimulus (Figures 32 and 36). At the highest amplitude position a voltage scan was carried out for each detector recording how the intensity of the signal generated changes when the bias voltage is shifted till it reaches full depletion value (Figures 33 and 39). After the results of the focus and voltage scans, the distance between the laser and the sample is kept and the signal from neighbor pads is measured in two different channels while the laser moves along from one pad to another. As the full depletion voltage changes with irradiation, several values from the voltage scan are studied

to find out precisely the value for the interpad gap distance. The interpad measurements are reported in Figures 34, 37 and 40.

The TCT results for the FBK W13 T4 detector irradiated at $8 \times 10^{14} \text{ n}_{\text{eq}}/\text{cm}^2$ are reported in Figures from 31 to 34, the results for the FBK W13 T4 detector irradiated at $15 \times 10^{14} \text{ n}_{\text{eq}}/\text{cm}^2$ are reported in Figures from 35 to 37 and the results for the FBK W13 T4 detector irradiated at $25 \times 10^{14} \text{ n}_{\text{eq}}/\text{cm}^2$ are reported in figures From 38 to 40.

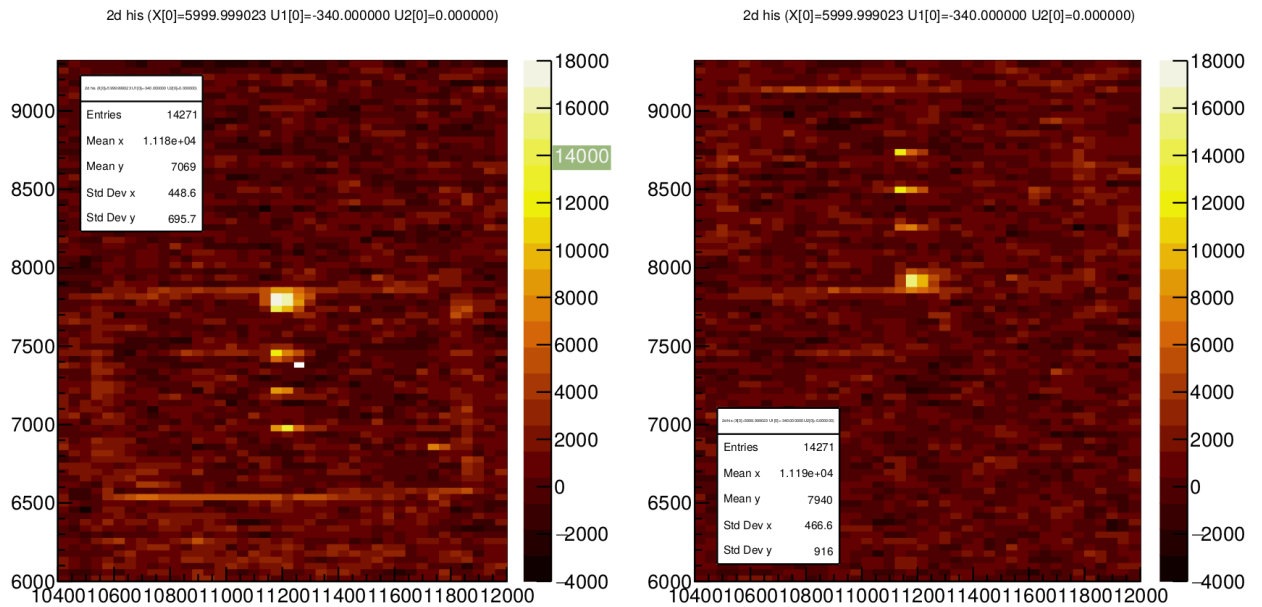


Figure 31. Rough scan of the surface of the FBK W13 T4 detector irradiated at $8 \times 10^{14} \text{ n}_{\text{eq}}/\text{cm}^2$. 2 neighbor pads are visible as well as the optic aperture. The Z axis shows the counts registered by the detector when the laser was illuminating that XY coordinate.

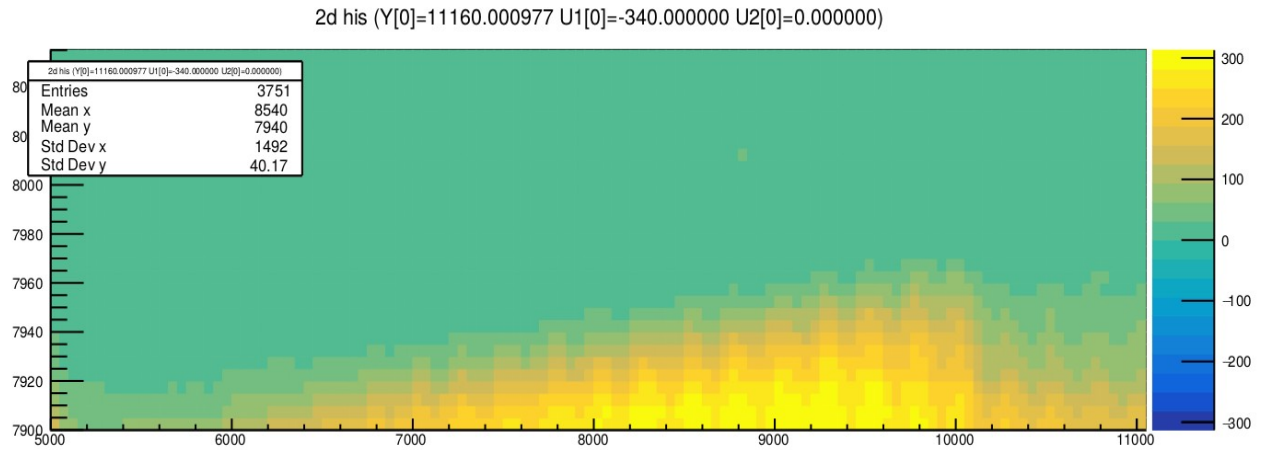


Figure 32. Focus scan of the surface of the FBK W13 T4 detector irradiated at $8 \times 10^{14} \text{ n}_{\text{eq}}/\text{cm}^2$. The X coordinate represents the distance between the laser and the sample. The Y coordinate lays parallel to the surface of the detector.

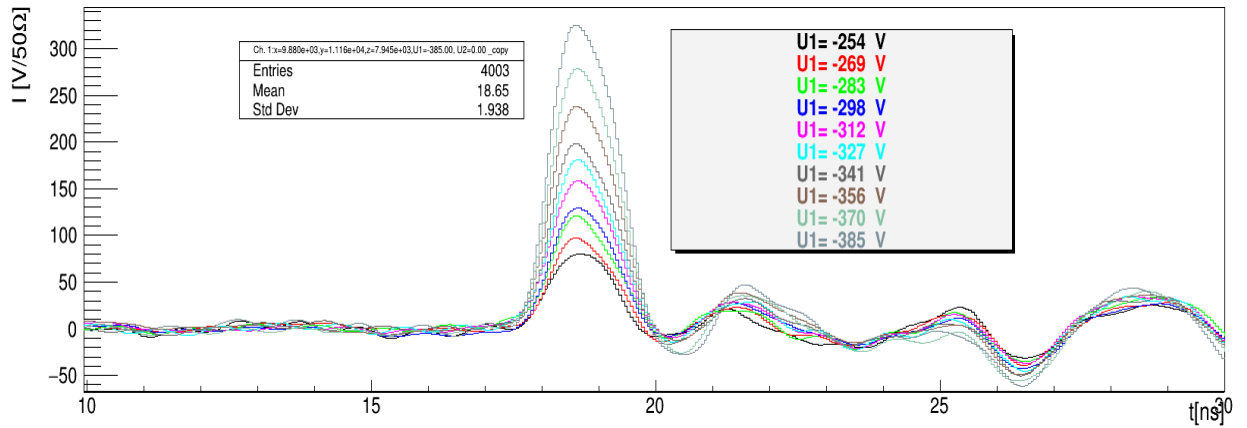


Figure 33. Voltage scan of the FBK W13 T4 detector irradiated at $8 \times 10^{14} \text{ n}_{\text{eq}}/\text{cm}^2$. The signal increments with the bias voltage and the impulse length is the time it takes for the carriers to go through the detector.

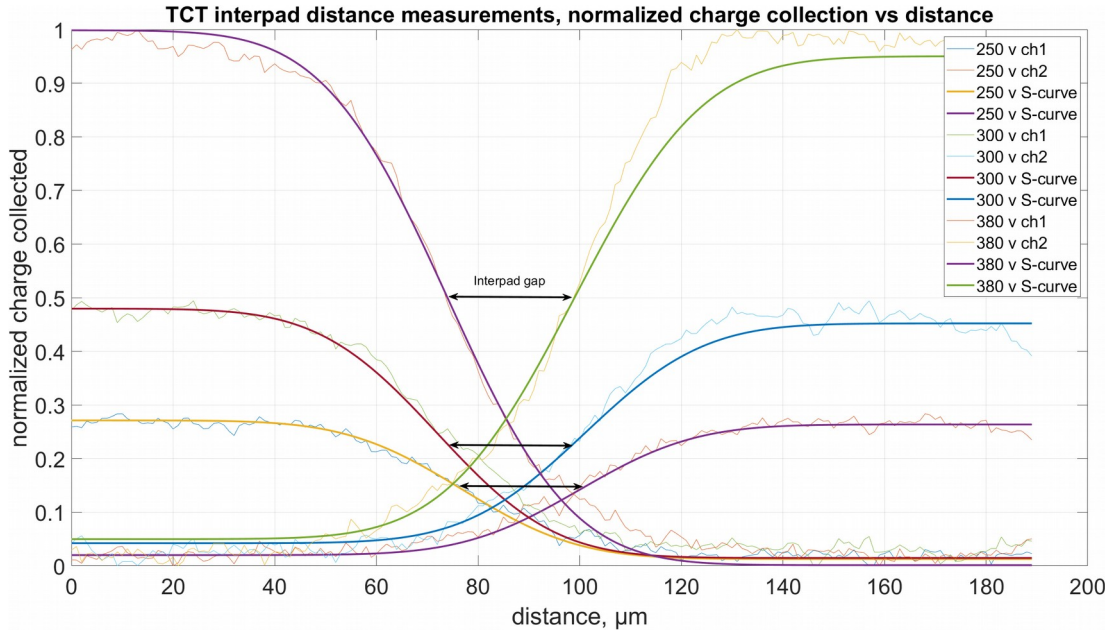


Figure 34. Interpad studies for the FBK W13 T4 detector irradiated at $8 \times 10^{14} \text{ n}_{\text{eq}}/\text{cm}^2$. S-curves error functions are placed as corrections for the data recorded. The parameter corresponding to the 50% of the signal amplitude for each curve marks the edge of the gain layer of each pad. Therefore, the interpad gap distance between channels can be measured from that point.

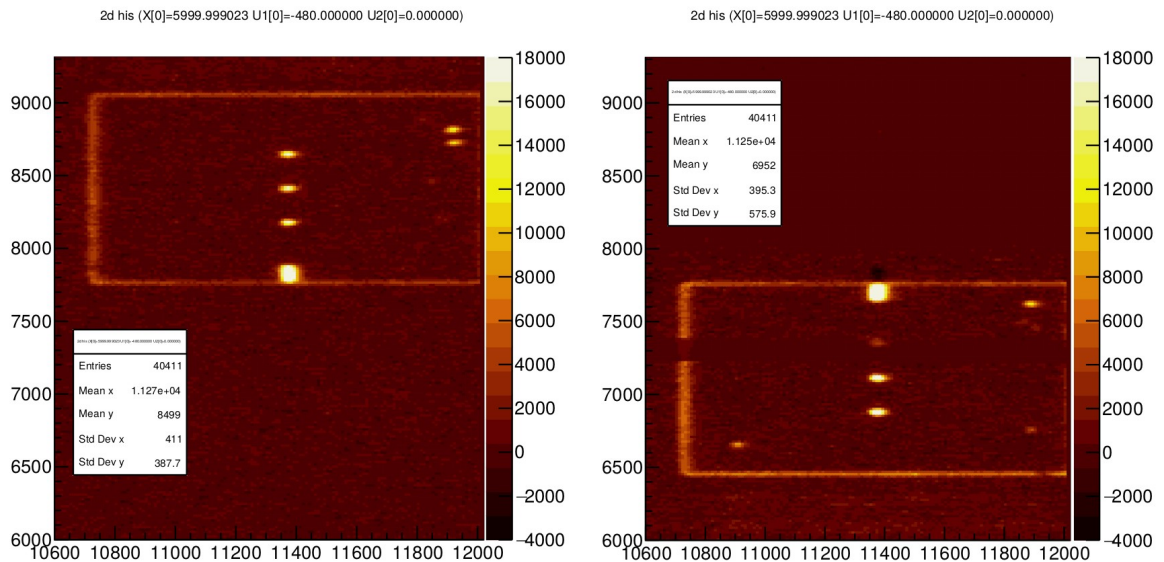


Figure 35. Rough scan of the surface of the FBK W13 T4 detector irradiated at $15 \times 10^{14} \text{ n}_{\text{eq}}/\text{cm}^2$. 2 neighbor pads are visible as well as the optic aperture. The Z axis shows the counts registered by the detector when the laser was irradiating that XY coordinate.

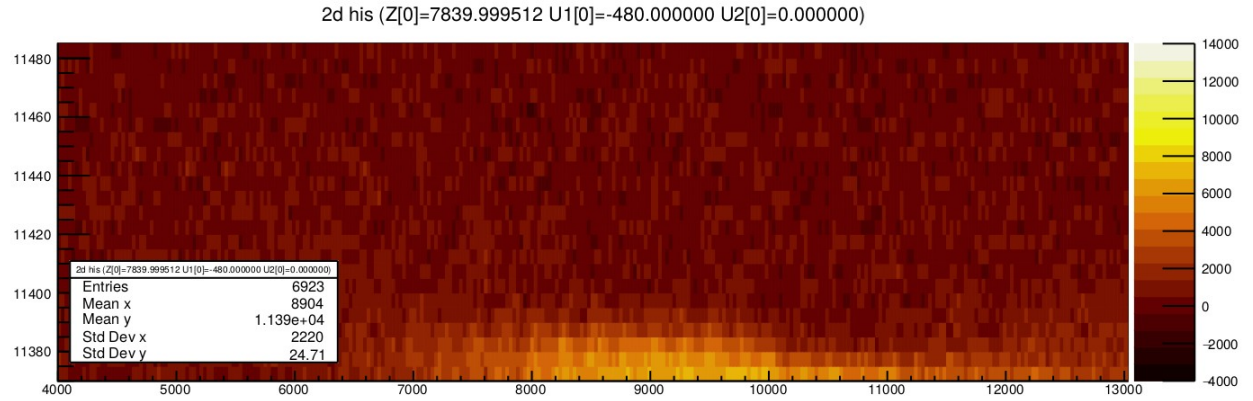


Figure 36. Focus scan of the surface of the FBK W13 T4 detector irradiated at $15 \times 10^{14} \text{ n}_{\text{eq}}/\text{cm}^2$. The X coordinate represents the distance between the laser and the sample. The Y coordinate lays parallel to the surface of the detector. The “sweet spot” can be found at the coordinate (8200 ,11385).

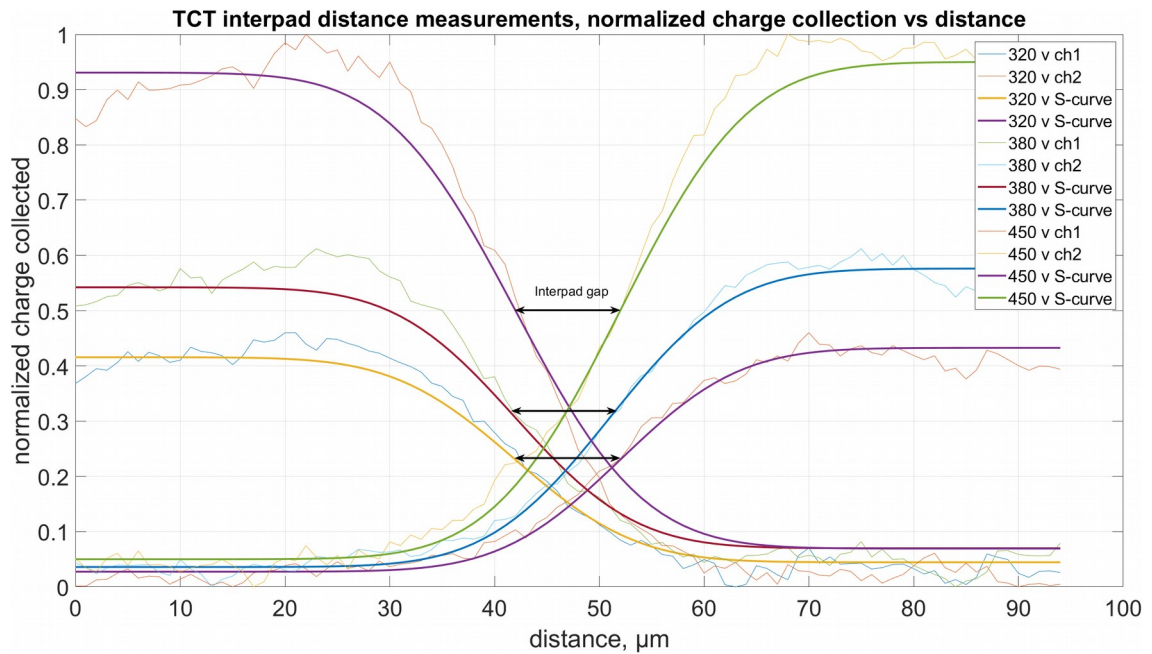


Figure 37. Interpad studies for the FBK W13 T4 detector irradiated at $15 \times 10^{14} \text{ n}_{\text{eq}}/\text{cm}^2$. S-curves error functions are placed as corrections for the data recorded. The parameter corresponding to the 50% of the signal amplitude for each curve marks the edge of the gain layer of each pad. Therefore, the interpad gap distance between channels can be measured from that point.

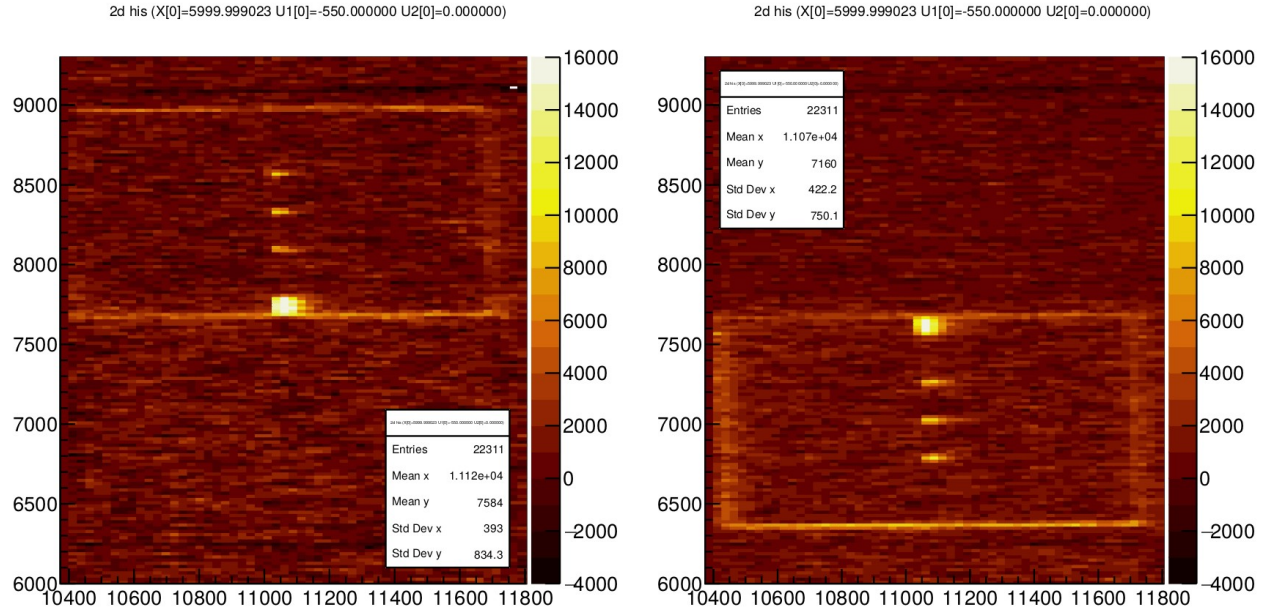


Figure 38. Rough scan of the surface of the FBK W13 T4 detector irradiated at $25 \times 10^{14} \text{ n}_{\text{eq}}/\text{cm}^2$. 2 neighbor pads are visible as well as the optic aperture. The Z axis shows the counts registered by the detector when the laser was irradiating that XY coordinate.

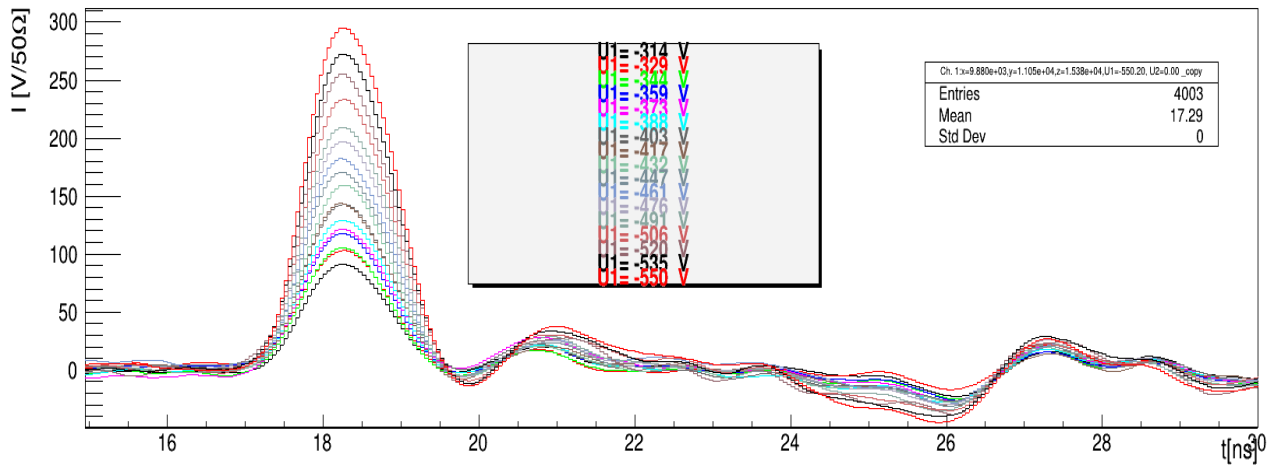


Figure 39. Voltage scan of the FBK W13 T4 detector irradiated at $25 \times 10^{14} \text{ n}_{\text{eq}}/\text{cm}^2$. The signal increments with the bias voltage and the impulse length is the time it takes for the carriers to go through the detector.

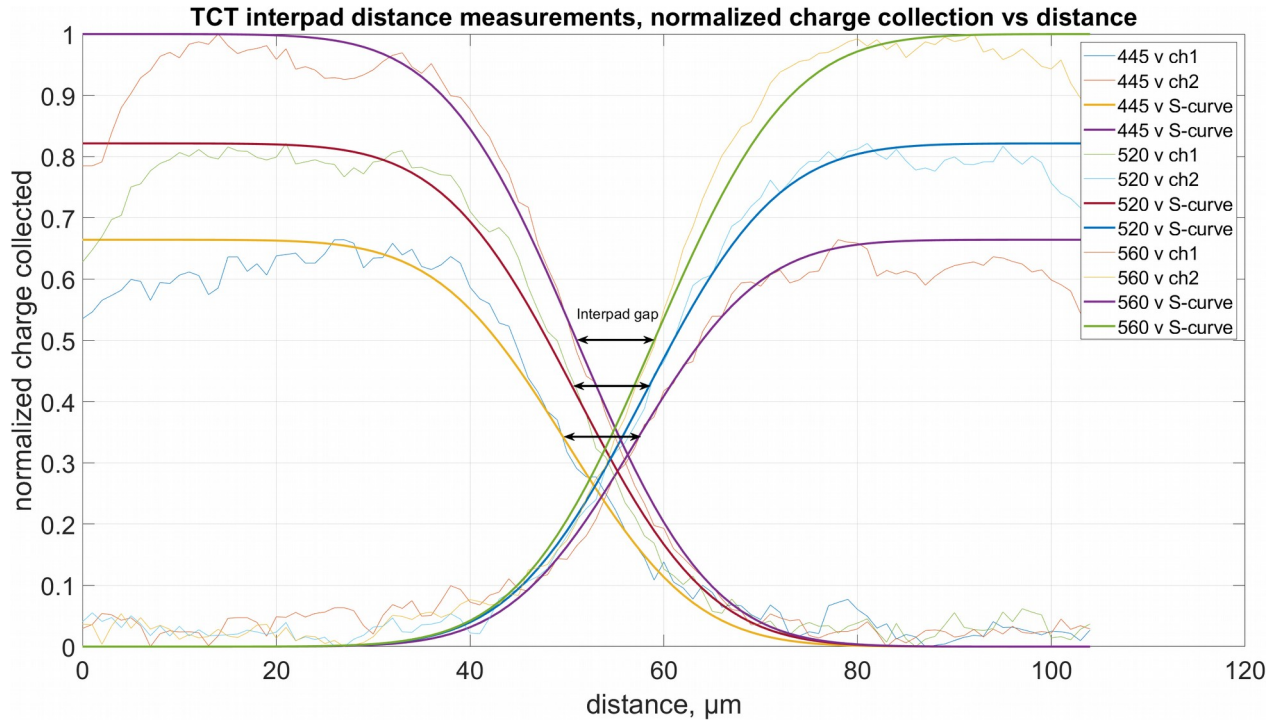


Figure 40. Interpad studies for the FBK W13 T4 detector irradiated at $25 \times 10^{14} \text{ n}_{\text{eq}}/\text{cm}^2$. S-curves error functions are placed as corrections for the data recorded. The parameter corresponding to the 50% of the signal amplitude for each curve marks the edge of the gain layer of each pad. Therefore, the interpad gap distance between channels can be measured from that point.

3.3. Annealing studies

Finally, annealing studies were carried out in three FBK and three HPK detectors to observe the level of improvement samples irradiated at difference fluences can reach by long periods of heating at 80°C . Results for the six samples are presented in Figures from 41 to 46.

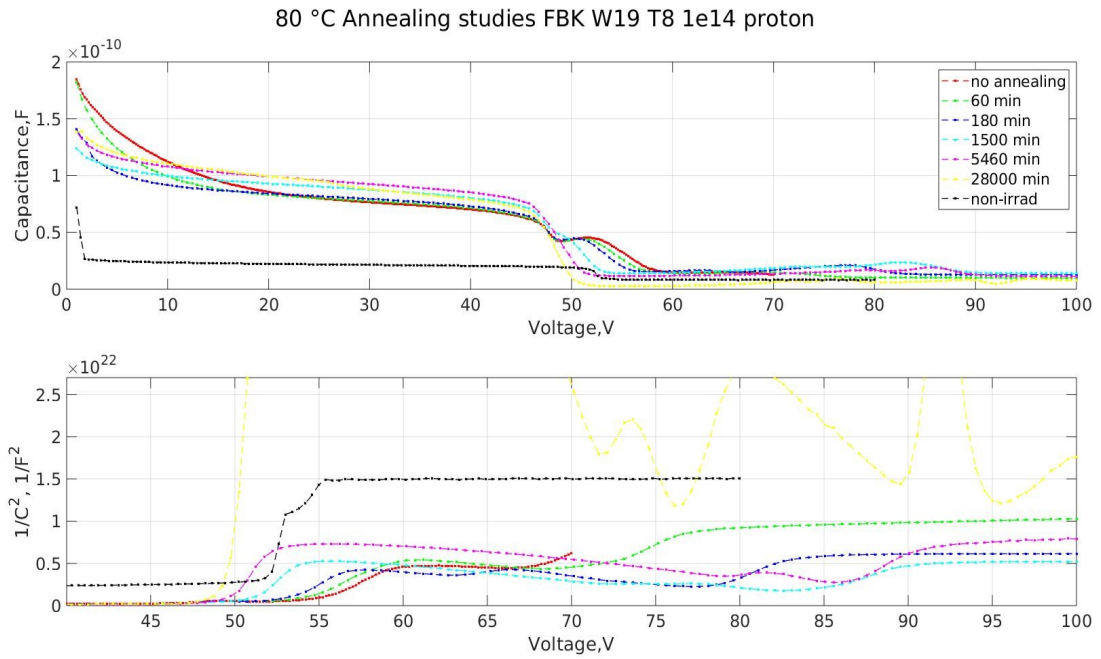


Figure 41. 80°C annealing studies of FBK W19 Type 8 sample irradiated at 1×10^{14} p/cm².

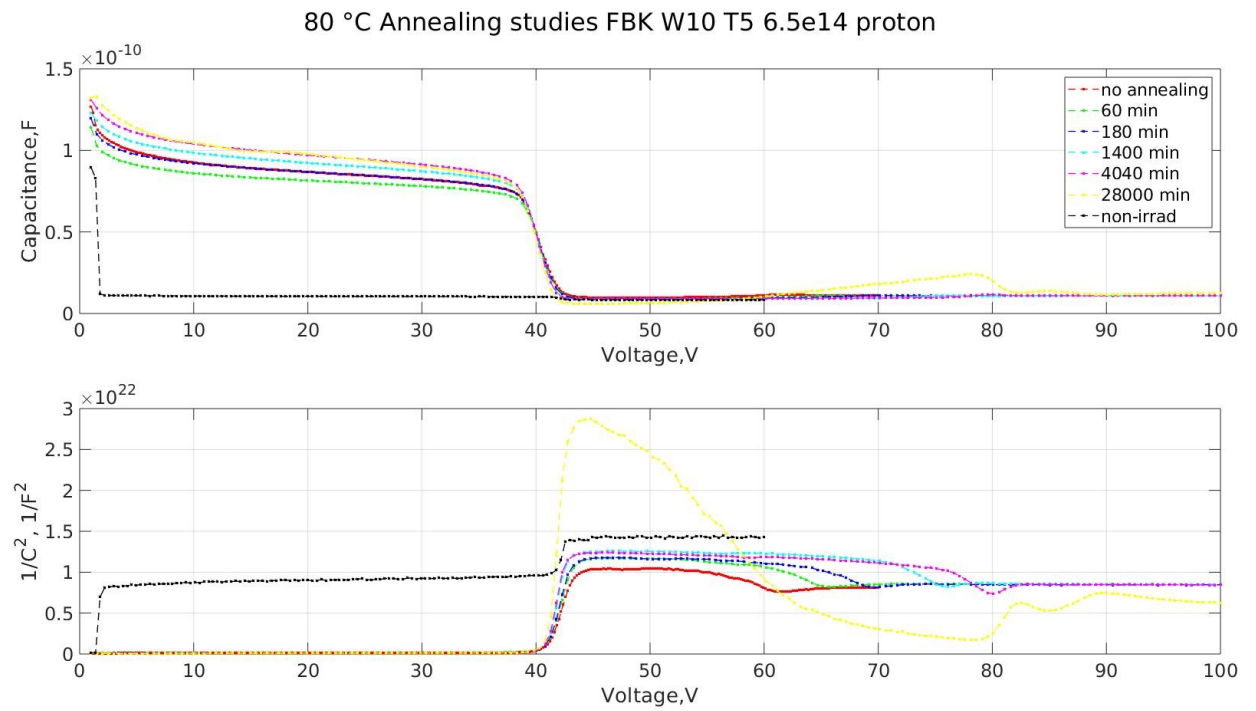


Figure 42. 80°C annealing studies of FBK W10 Type 5 sample irradiated at 6.5×10^{14} p/cm².

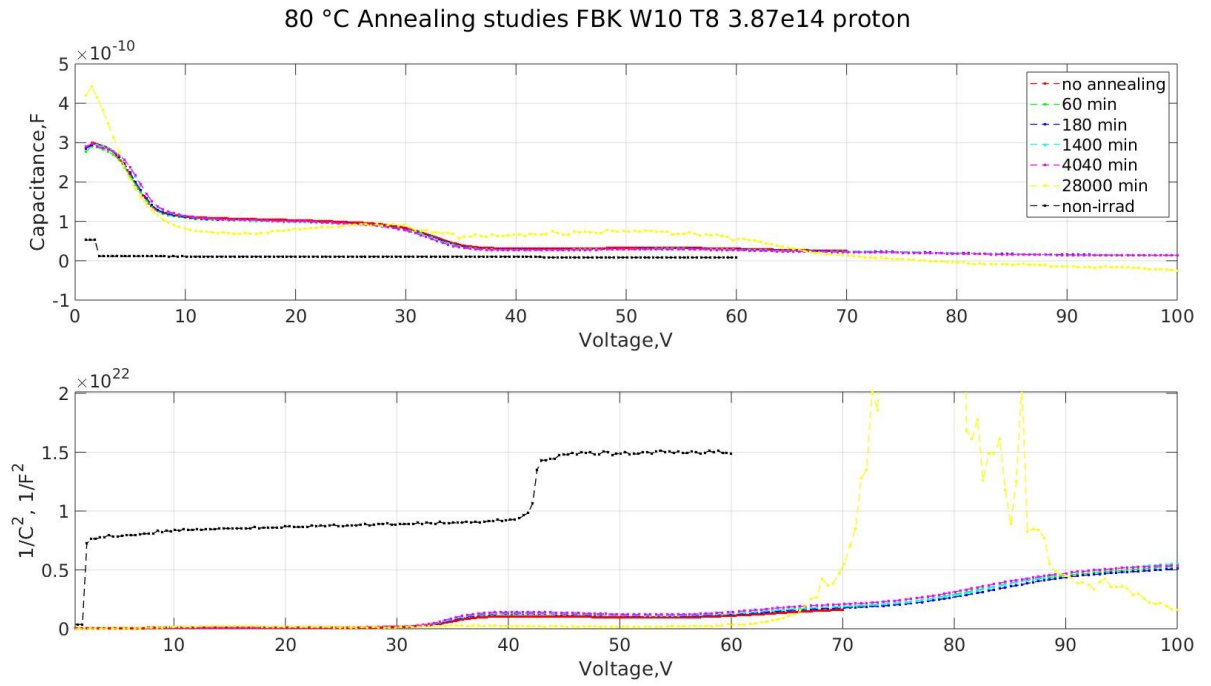


Figure 43. 80°C annealing studies of FBK W10 Type 8 sample irradiated at 3.87×10^{14} p/cm².

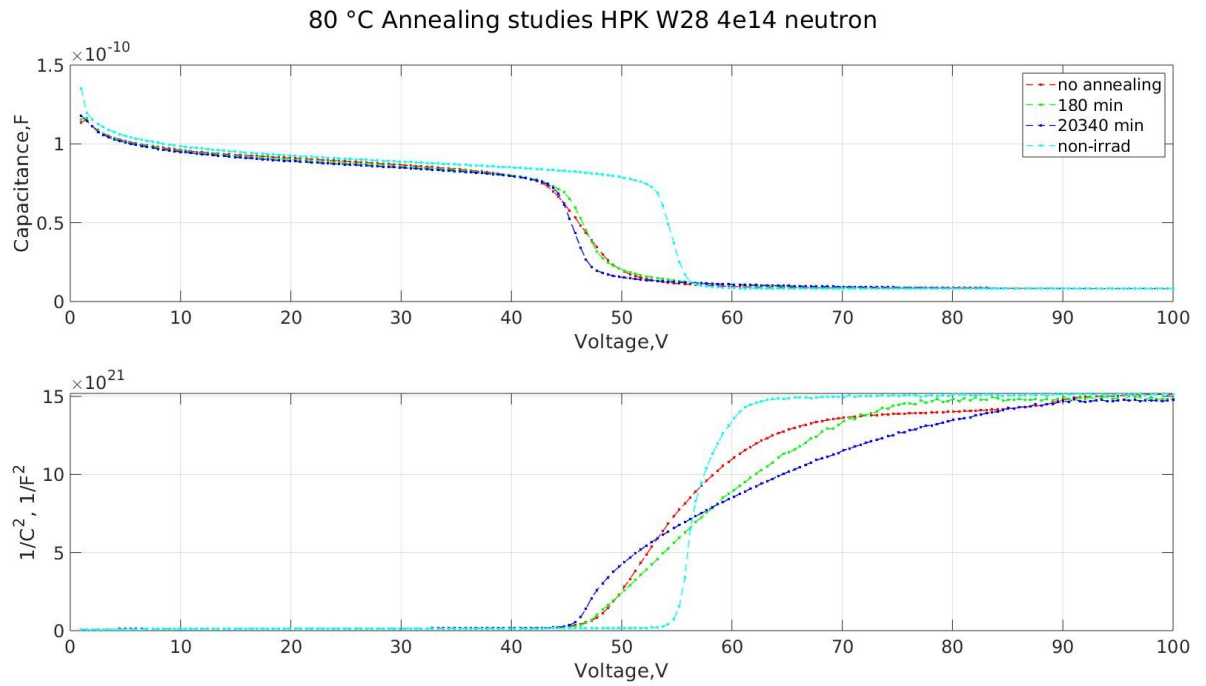


Figure 44. 80°C annealing studies of HPK W28 sample irradiated at 4×10^{14} n_{eq}/cm².

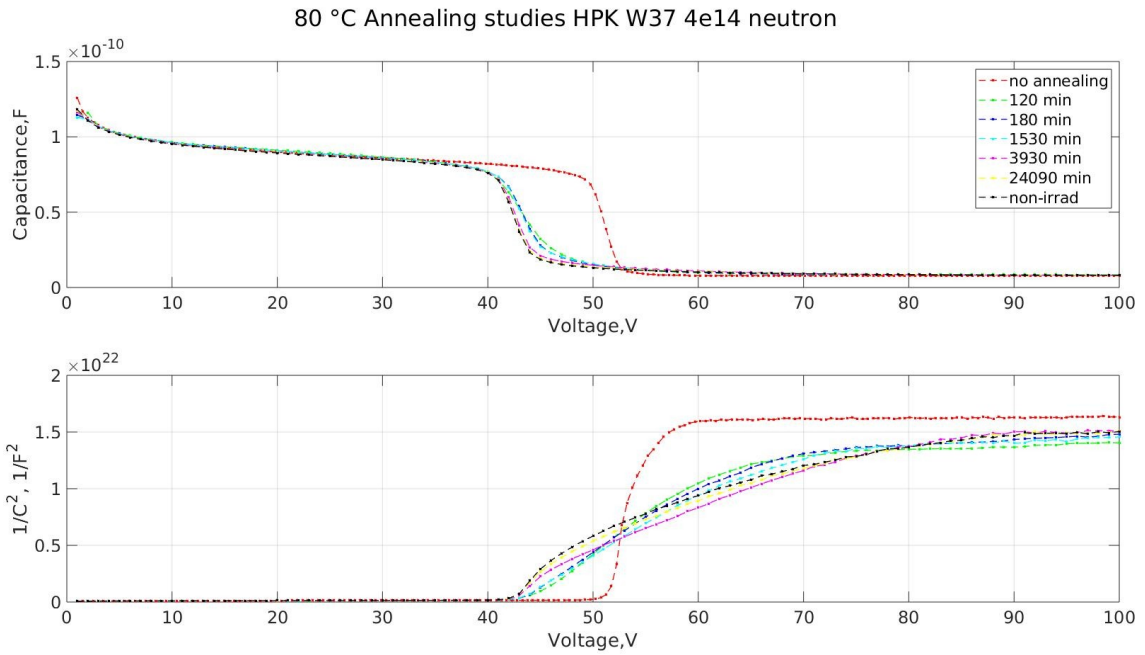


Figure 45. 80°C annealing studies of HPK W37 sample irradiated at $4 \times 10^{14} \text{ n}_{\text{eq}}/\text{cm}^2$.

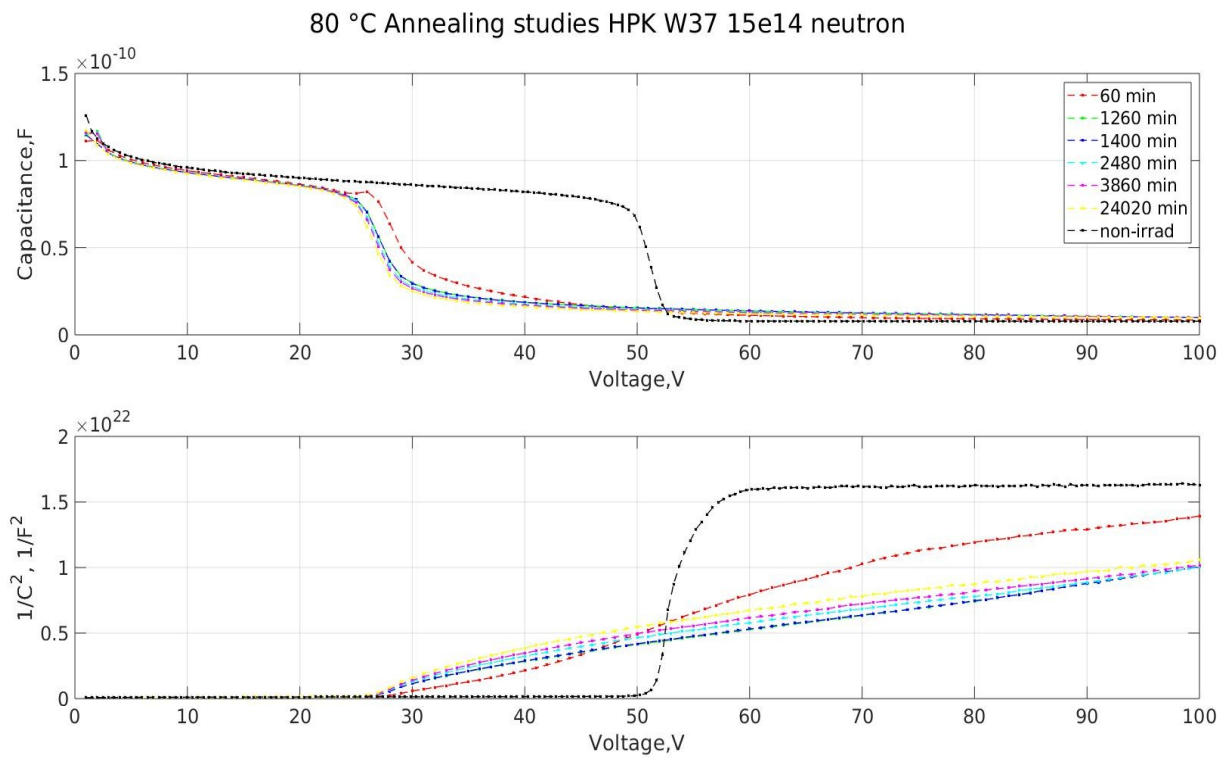


Figure 46. 80°C annealing studies of HPK W37 sample irradiated at $15 \times 10^{14} \text{ n}_{\text{eq}}/\text{cm}^2$.

3.4. Discussion

The accumulation of charge inside the detector due to the SCR is responsible for the pn-junctions to act as a capacitor. Thus, the capacitance of the detector value can be calculated through the formula for a parallel capacitor:

$$C = \epsilon \frac{A}{d} = \frac{dQ}{dV} \quad (23)$$

Where d is the distance between the plates, A is the area of these plates and ϵ is the dielectric constant of the material (silicon) in between the plates. The depleted region, emptied from carriers, works as the insulator of the capacitor thus the depletion region size will replace d in equation 23. Therefore, if we take the formula for the depletion region from (16) we obtain:

$$C = \sqrt{\frac{q A \epsilon N}{2V}} \quad (24)$$

Where N is the effective dopant concentration and V the bias voltage. From here the Hillibrand-Gold formula allows us to define the effective dopant concentration [49]:

$$N(W) = \frac{-C^3}{A^2 q \epsilon} / \left(\frac{dC}{dV} \right), \quad \text{or} \quad N(W) = \left(\frac{2}{A^2 q \epsilon} \right) / \left(\frac{d(\frac{1}{C^2})}{dV} \right) \quad (25)$$

Meaning that the value of the C-V curves in the inflection points, or what is the same, the slope of the $1/C^2$ curves at the inflection points correspond to the full depletion voltage for each pn-junction, i.e. for the gain layer and for the detector bulk.

With (25) and (23), we can find the doping profile of the detectors as shown in Figure 47.

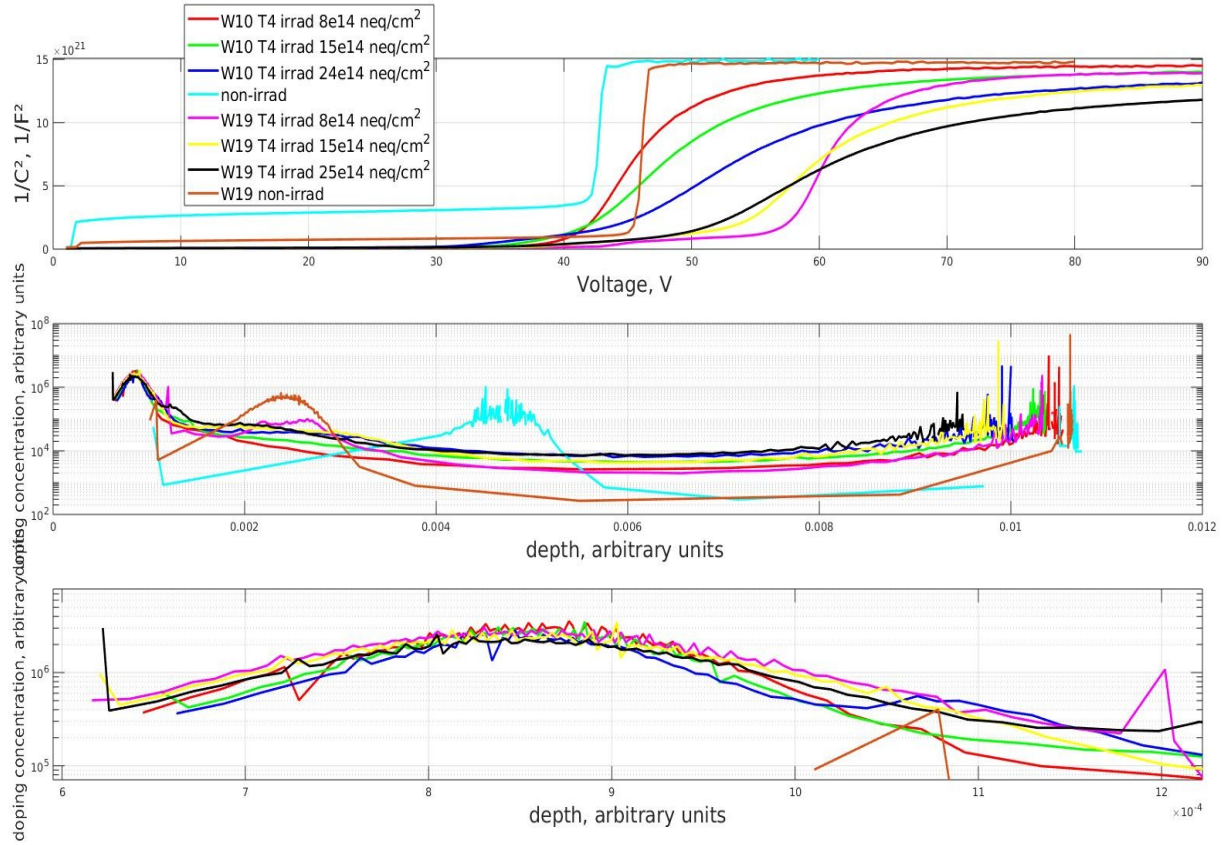


Figure 47. $1/C^2$ graph (up), complete doping profile of FBK W10 T4 neutron irradiated samples (middle) and zoomed (down).

As it can be observed, doping values slightly decrease with radiation due to the displacement of the dopant inside the bulk and the multiplication layer. It is important to mention that this phenomenological approach to calculate the doping profile is based on the assumption that the pn-junction is abrupt and uniform along the $1.3 \times 1.3 \text{ mm}^2$ area of the pad, what in reality has proven to be unprobable, due to the mentioned displacement and defect clusters formation.

The doping profiles for the measured HPK C-V characteristics are reported in Figures from 48 to 51.

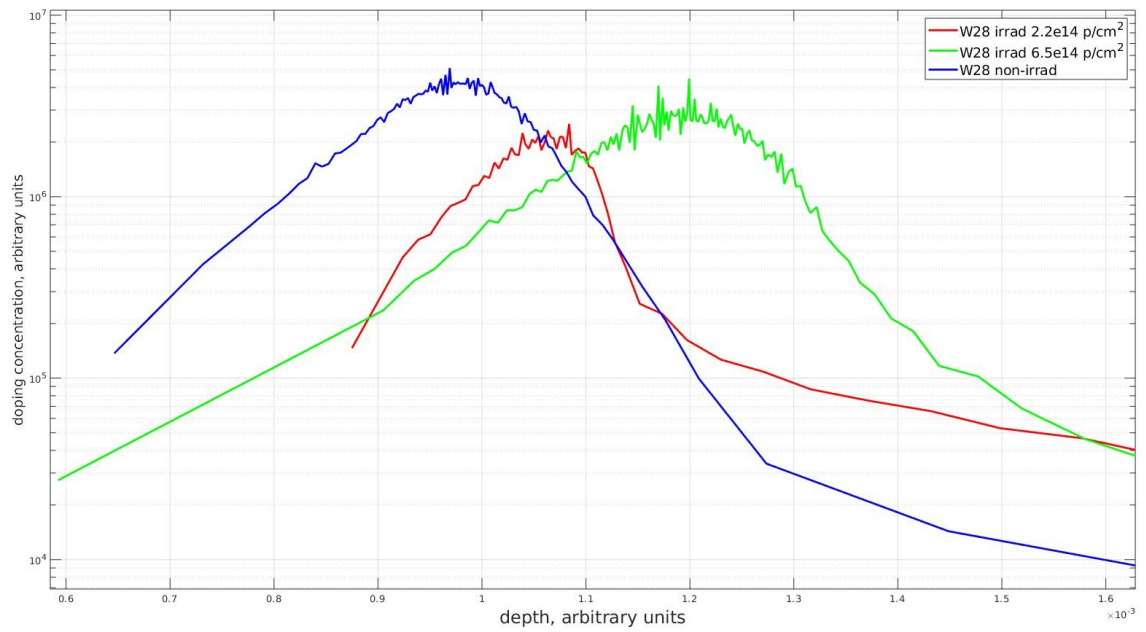


Figure 48. Doping profile of HPK W28 proton irradiated samples zoomed.

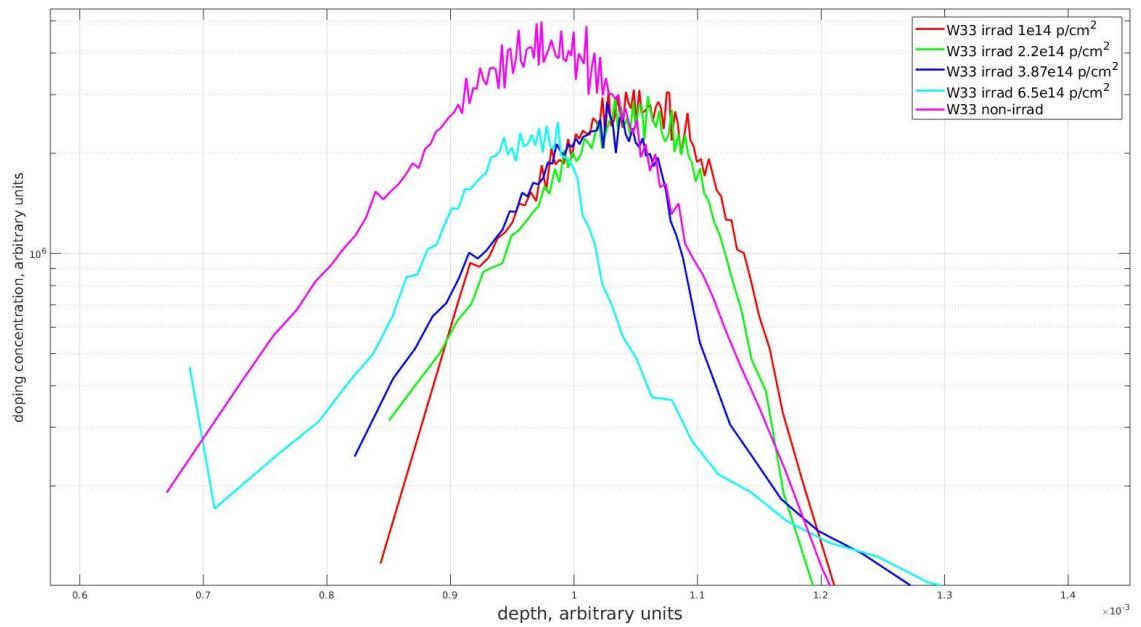


Figure 49. Doping profile of HPK W33 proton irradiated samples zoomed.

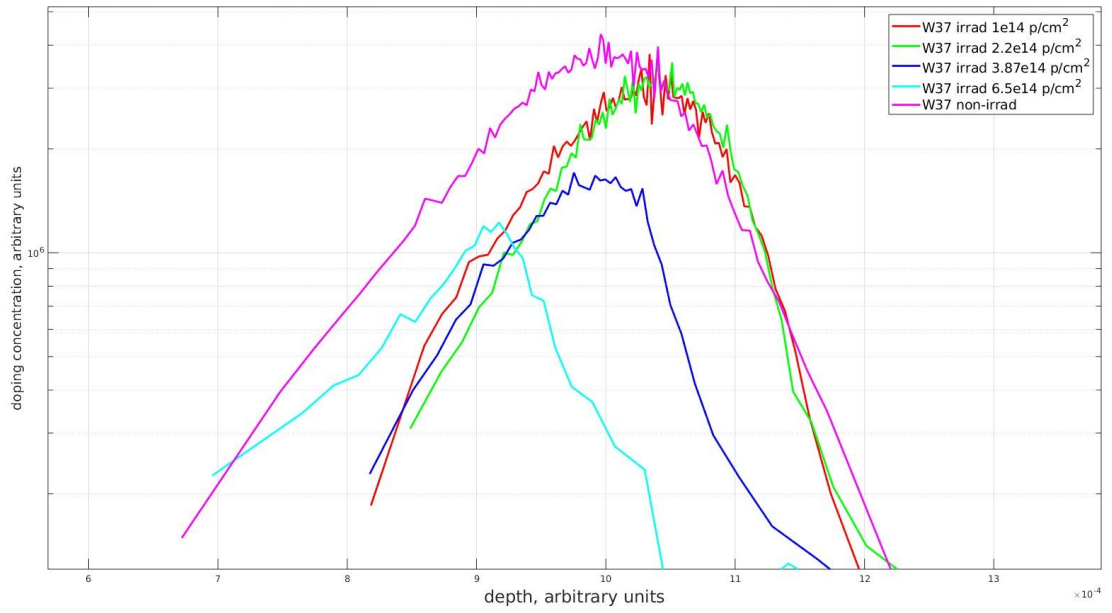


Figure 50. Doping profile of HPK W37 proton irradiated samples zoomed.

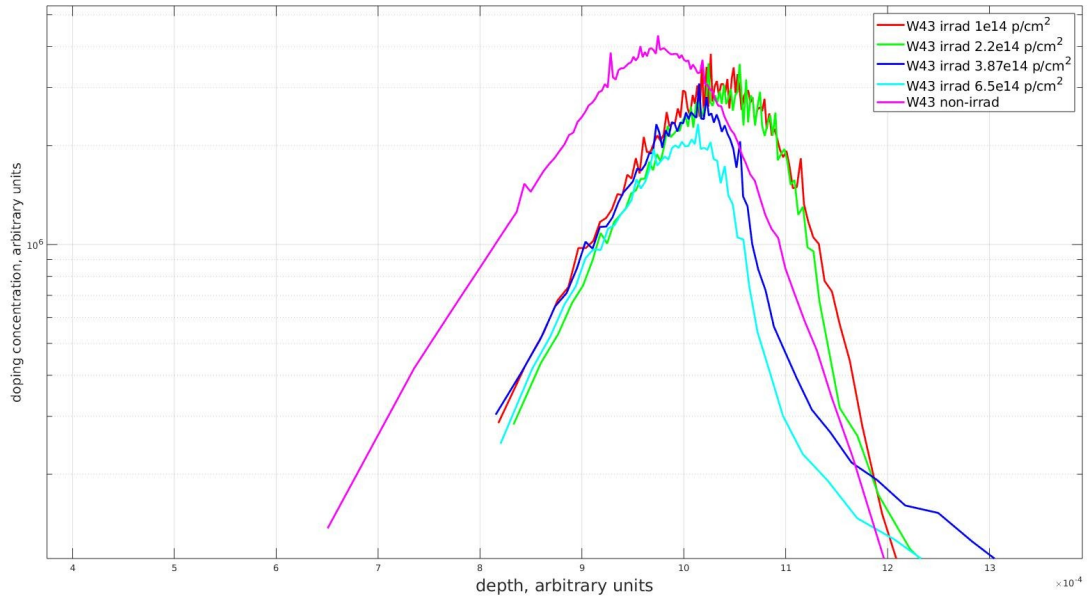


Figure 51. Doping profile of HPK W43 proton irradiated samples zoomed.

The depletion voltage for the gain layer and the bulk of the detector correspond to the voltages where an inflection point is found at the C-V curves, i.e. points where the line described by the “plain” C sections intersect with the line with the highest slope absolute value. To make this value more clear it is recommended to plot a $d(1/C^2)/dV$ vs V_{bias} curve.

The V values for the half amplitude of the peaks mark the exact values of the depletion voltage like its exemplified in Figure 54.

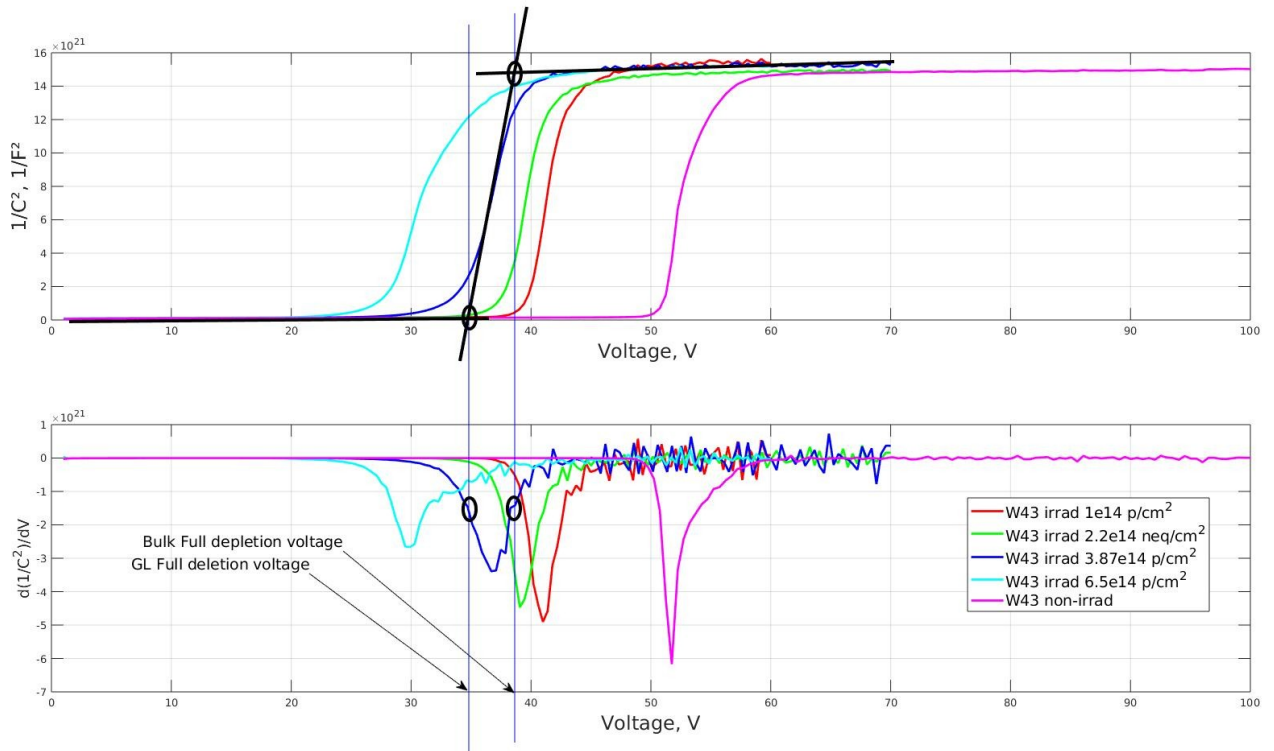


Figure 54. Example of depletion voltage identification. Up, $1/C^2 - V$ curve of HPK W43 samples. Down $d(1/C^2)/dV$ curve for the same samples. Full depletion voltages for one sample are indicated in the figure.

The values for depletion voltage and highest calculated effective doping concentration are reported in table 3.

Table 3. Depletion voltage and highest calculated values for the samples measured.

Detector	Parameter		
	Depletion voltage, V		Max. doping concentration , 10 ⁶ ,AU
FBK			
W 10	Gain layer	Bulk	
T4 no-irradiated	42.87	43.12	0.1

Detector	Parameter		
T4 $8 \times 10^{14} \text{ n}_{\text{eq}}/\text{cm}^2$	41.92	48.58	2.9
T4 $15 \times 10^{14} \text{ n}_{\text{eq}}/\text{cm}^2$	41.53	43.45	2.5
T4 $25 \times 10^{14} \text{ n}_{\text{eq}}/\text{cm}^2$	43.51	57.02	2.2
W19			
T4 no-irradiated	45.57	46.32	0.5
T4 $8 \times 10^{14} \text{ n}_{\text{eq}}/\text{cm}^2$	57.72	62.49	2.5
T4 $15 \times 10^{14} \text{ n}_{\text{eq}}/\text{cm}^2$	54.24	62.52	2.4
T4 $25 \times 10^{14} \text{ n}_{\text{eq}}/\text{cm}^2$	50.27	67.3	2.1
W10			
T5 $2.2 \times 10^{14} \text{ p}/\text{cm}^2$	39.44	43.98	~
T5 no-irradiated	41.69	42.4	~
T9 $2.2 \times 10^{14} \text{ p}/\text{cm}^2$	40.70	44.96	~
T9 no-irradiated	41.23	42.3	~
T5 $6.5 \times 10^{14} \text{ p}/\text{cm}^2$	41.1	43.15	~
T7 $6.5 \times 10^{14} \text{ p}/\text{cm}^2$	~	~	~
T7 no-irradiated	41.45	42.3	~
T9 $6.5 \times 10^{14} \text{ p}/\text{cm}^2$	42.1	42.7	~
T8 $3.87 \times 10^{14} \text{ p}/\text{cm}^2$	~	~	~
T8 no-irradiated	41.9	42.5	~
W19			
T8 $1 \times 10^{14} \text{ p}/\text{cm}^2$	~	~	~
T8 no irradiated	51.5	52.1	~
T7 $2.2 \times 10^{14} \text{ p}/\text{cm}^2$	~	~	~

Detector	Parameter		
T7 no irradiated	52.3	52.8	~
T7 6.5×10^{14} p/cm ²	52.06	54.43	~
T8 3.87×10^{14} p/cm ²	~	~	~
T4 6.5×10^{14} p/cm ²	43	53.05	~
T4 no irradiated	51.8	52.5	~
HPK			
W28 2.2×10^{14} p/cm ²	27.7	32.6	2
W28 6.5×10^{14} p/cm ²	53.3	54.9	3
W28 no irradiated	55	56.4	4
W33 1×10^{14} p/cm ²	36.3	40.02	3
W33 2.2×10^{14} p/cm ²	31.7	34.9	2.8
W33 3.87×10^{14} p/cm ²	33	36.4	2.5
W33 6.5×10^{14} p/cm ²	29.8	37.9	2.1
W33 no irradiated	54.1	55.3	4.1
W37 1×10^{14} p/cm ²	38.7	41.4	3.1
W37 2.2×10^{14} p/cm ²	38.7	41.4	3
W37 3.87×10^{14} p/cm ²	24	35.1	1.5
W37 6.5×10^{14} p/cm ²	17.6	27.9	1.1
W37 no irradiated	51.6	53	4
W43 1×10^{14} p/cm ²	39.9	42.2	3
W43 2.2×10^{14} p/cm ²	37.9	40.05	2.8
W43 3.87×10^{14} p/cm ²	34.6	38.3	2.5
W43 6.5×10^{14} p/cm ²	38.1	40.5	2

Detector	Parameter		
W43 no irradiated	51	52.3	4

Comparing the table values and the graphics from irradiated and non irradiated samples a decrement in the value of the GL depletion voltage can be observed as a tendency while the irradiation fluence value increases. The uniform pn-junction approach was not suitable for proton irradiated samples, due to the irregularities in their C-V curves what is a sign of high radiation damage or a not homogeneous pn-junction manufacturing. In proton irradiated samples, fluences of 6.45×10^{14} p/cm² and higher in samples from the types 7 and 9 made them loose completely their LGAD properties and behave like PIN diodes, for W10 as well as for W19. Even in these cases, the capacitance values do not decrease less sharply than in the other samples what proves a reduction in the resistance of the detector due to radiation damage and gives a hint about the presence of thermal donors in the bulk.

Type 8 detectors showed a poor performance in W10 as well as in W19 as they became highly unstable after receiving radiation dosages of 3.87×10^{14} p/cm². Perhaps C-V values were inside the valid range for the W10, however the irregular values the detector showed during tests are not suitable for a precise detector in future operation.

The best performance for each type of wafer was presented by samples of the 5 type in W10 and type 4 for W19. Samples irradiated with neutrons were all from the type 4 as studies made on the previous batch of FBK detectors (UFSD 3.1) showed them as the most promising ones [21].

The rising value of capacitance when irradiation fluence values increase can be explained by the composition of the FBK samples bulk. In the process of fabrication, the doping level is kept at the minimum almost as an intrinsic bulk. Also, the Czochralski method of fabrication allows the presence of impurities such as oxygen inside the ingot. The oxygen present in the lattice acts as a thermal donor, freeing electrons when the detector is heated or acting as a carrier donor inside the p-type lattice. This is reflected in the C-V graphs as an increment of the capacitance in accordance with the increase of the irradiation value because the process of depletion starts then by depleting the electrons

present in the bulk and not the holes (the bulk would be space charge inverted to n⁺-type). Parasitic capacitance comes from the undesired interaction of the carriers with the guard ring. As the electrons move from the bulk to their respective electrode they can flow to other pads as the interpad protection is designed for controlling holes but not electrons. This means also that the only mechanism of control for electrons is the interpad gap as the effective size of the detector's active region is not delimited anymore by the gain layer nominal size but by the common p-type electrode shared by the pads [50].

The increment in the radiation damage displaces more acceptors from the bulk reducing the hole concentration and increasing the electron charge collection represented in the C-V characteristics. Radiation can also damage the GL obtaining this way the PIN diode-like behavior of the samples.

The reduction of the GL full depletion voltage with the increasing irradiation values is due to the decrement of the donor concentration. The reduction of acceptors means a reduction of carriers, thus a lower voltage required for a full depletion. This also means a reduction in the gain.

HPK samples have proven to be more efficient and stable than the FBK samples. All the samples kept their LGAD properties, presented organized curves and kept the maximum capacitance values almost the same after the highest radiation dosage was applied to them. In contrast with the FBK samples, the capacitance values of the samples tend to decrease with irradiation, what is expected as the charge collection is reduced due to radiation damage. However, FBK samples' bulk full depletion voltages increase with irradiation, what is also expected to happen as more voltage is required to empty completely the bulk from trapped carriers or local parasitic electric field zones. This is not seen in the majority of HPK samples as their bulk full depletion voltage is also reduced with irradiation together with the GL full depletion voltage value.

Using the formula for acceptor removal the radiation hardness was quantified for the studied detectors:

$$N_{eff} \approx N_{eff_0} * e^{-c \phi} \quad (26)$$

Here, N_{eff0} is the dopant concentration when the detector was not irradiated, ϕ is the fluence value and c is the acceptor removal coefficient, whose value determines the detector radiation tolerance.

The amount of acceptor removed increases with the irradiation fluence. After quantifying the losses it was observed that all samples' acceptor removal coefficients laid less than one order of magnitude over the one expected to be considered radiation hard enough for operation. However, the sample that gets the closest to this condition is the HPK W37. According to the registered results, proton irradiated HPK samples from wafer 28 suffered a removal of 25% and 50% of acceptors in the GL, W33 suffered a reduction of 26.8%, 31.7%, 39% and 48.8% of acceptors, W37 lost 22.5% , 25%, 62.5% and 75% and W43 25%, 30%, 37,5% and 50% . The stability and good operational behavior are good signs for further development of HPK samples.

After the analysis of the radiation resistance was made on these samples, the stability test for type 4 samples was carried out. As shown in rough scan figures, detectors responded properly to the laser stimulus without breaking out or burning. These rough scan tests work as a stability test as they are carried out during at least 8 hours of constant irradiation while recording each pixel of information. The results of the measurements showed the response of each pad to the laser, without exciting any neighboring pad which discards any charge trespass between pads while in operation.

Respectively, rough scans showed the location of the optical apertures in the next coordinates: for the FBK W13 T4 irradiated at 8×10^{14} p/cm², in the X range of 11150 μ m -11250 μ m and in the Y range of 7750 μ m -7850 μ m for the first pad and 7850 μ m – 7950 μ m for the second pad. For the FBK W13 T4 irradiated at 15×10^{14} p/cm², in the X range of 11350 μ m -11450 μ m and in the Y range of 7750 μ m -7850 μ m for the first pad and 7650 μ m– 7750 μ m for the second pad and finally, for the FBK W13 T4 irradiated at 25×10^{14} p/cm², in the X range of 11000 μ m -11100 μ m and in the Y range of 7650 μ m - 7800 μ m for the first pad and 7650 μ m – 7550 μ m for the second pad.

The maximum intensity “sweet” focus coordinates for the 3 detectors were: for the FBK W13 T4 irradiated at 8×10^{14} p/cm² at (10150 ,7940) and for the FBK W13 T4 irradiated at 15×10^{14} p/cm² at (8200 ,11385) and finally for the FBK W13 T4 irradiated at 25×10^{14} p/cm² was roughly estimated the same as for the irradiated at 15×10^{14} p/cm² as this

two samples were placed in the same way in the sample holder and thus the same z value was kept.

For interpad studies the measured data is represented together with an s-curve fit (error) function as the data is composed by the superposition of two different types of functions: The Gaussian function from the laser beam intensity and the step function from the active region edge profile (figure 55). The error function formula depends on four parameters:

$$f(x) = \frac{a}{2} + \left\{ \frac{b}{2} * \operatorname{erf} \left[\frac{2 * \sqrt{2} (x - c)}{d} \right] \right\} \quad (27)$$

Where a is the signal maximum amplitude, b is the slope of the curve at the inflection point, c is the median of the curve and d is the standard deviation (σ). Therefore, the difference between channel's 1 and channel's 2 fit functions' c parameters can be interpreted as the interpad gap.

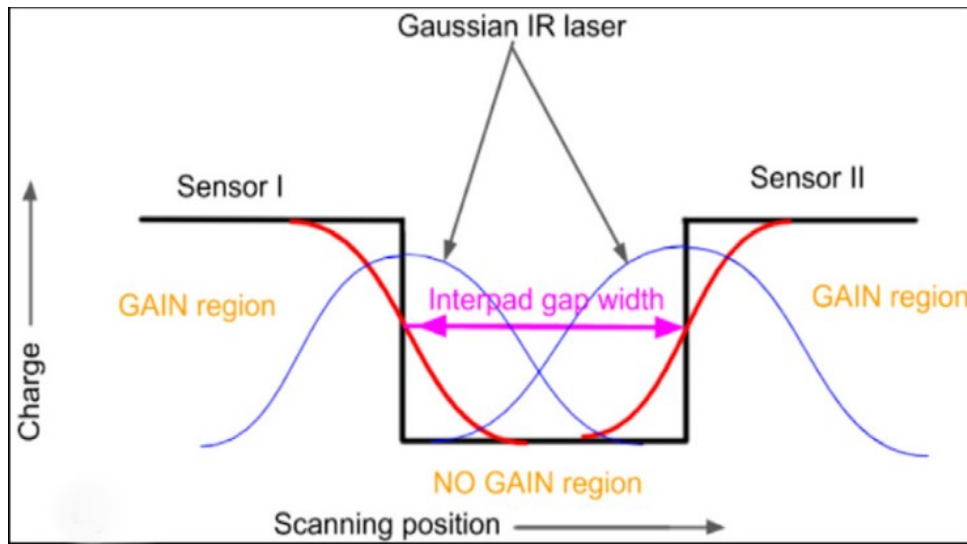


Figure 55. Function superposition at interpad studies. As the Gaussian function decreases till the 50% of its maximum, the center of the laser beam moves from 1 pad to the other [51].

The interpad studies showed a very close value of the interpad gap to the nominal. For type 4 samples the nominal distance is about 24 μm . The measured values for the interpad gap were 24 μm for the $8 \times 10^{14} \text{ n}_{\text{eq}}/\text{cm}^2$ irradiated sample, 10 μm for the $15 \times 10^{14} \text{ n}_{\text{eq}}/\text{cm}^2$ irradiated sample and 8 μm for the $25 \times 10^{14} \text{ n}_{\text{eq}}/\text{cm}^2$ irradiated sample. This can be

explained by the displacement of acceptor atoms from the lattice, moving in every direction and reducing the acceptor concentration of the gain layer and reducing the size of the interpad gap at the same time. The neighbor pads were still isolated even at an interpad gap size of 8 μm what increases type 4 detectors operative life and radiation resistance qualification. If we consider the area of the pads the whole detector area and the only no gain region is the distance between pads, then the improvement in the fill factor of the detector will be around 1.22% what in a larger scale would mean a significant increment in performance.

Annealing studies revealed that even after two weeks of annealing, a detector can still show signs of repairing damage, up to a state pretty similar to the non-irradiated one as the HPK W37 irradiated at $4 \times 10^{14} \text{ n}_{\text{eq}}/\text{cm}^2$ fluences. However, this is only true for low irradiation values. For FBK samples, specially FBK W10 T8 irradiated at $3.87 \times 10^{14} \text{ n}_{\text{eq}}/\text{cm}^2$ not only the effect was minimal was observed that an extensive exposure to the heat can also trigger the diffusion mechanism of the impurities inside the material changing the doping concentrations along the detector and leaving it useless. The increment in the capacitance value with the annealing time for the FBK samples confirms the presence of thermal donors inside the FBK detector structure as all detectors increased their capacitance values instead of getting values closer to the non irradiated characteristics. Annealing studies also confirmed that HPK samples present a higher thermal tolerance than FBK samples and are more suitable for use in the accelerator.

The changes in the dopant concentration and depletion voltages of the annealing samples are compiled in Table 4. As expected, samples improved their values for full depletion voltage and the C-V curves repaired undesired inflection points due to carrier trapping.

Table 4. Depletion voltage and highest calculated values for the annealed samples.

Sample/Annealing time	Depletion voltage, V		Max. doping concentration , 10^6 AU
	Gain layer	Bulk	
FBK W 19 T8 $1 \times 10^{14} \text{ p}/\text{cm}^2$			
No annealed	56.2	58.6	6.5
60 min	55	59.2	6

Sample/Annealing time	Depletion voltage, V		Max. doping concentration , 10 ⁶ AU
180 min	53.8	56.2	5
1500 min	51.3	53.2	4.8
5460 min	49.8	51.6	4.8
28000 min	50.1	52.6	5
Non-irradiated	52	52.8	1.5
FBK W 10 T5 6.5x10 ¹⁴ p/cm ²	Bulk	Gain layer	
No annealed	41.2	43	1.1
60 min	40.9	42.8	1.1
180 min	41	42.7	1.1
1400 min	41.1	42.2	1.1
4040 min	40.8	42.2	1.1
28000 min	41	42.3	1.8
Non-irradiated	~	~	1
FBK W 10 T8 3.87x10 ¹⁴ p/cm ²	Bulk	Gain Layer	
No annealed	32.5	36.8	4.4
60 min	32.6	36.6	3.6
180 min	32.6	36.6	3.9
1400 min	32.8	36.4	4.4
4040 min	32.3	36.5	4.6
28000 min	~	~	5.1
Non-irradiated	41.9	42.6	11

Sample/Annealing time	Depletion voltage, V		Max. doping concentration , 10 ⁶ AU
	Bulk	Gain Layer	
HPK W28 4x10 ¹⁴ n _{eq} /cm ²	Bulk	Gain Layer	
No annealed	47.8	60	4.5
180 min	46.5	~	4.5
28000 min	45.8	48.8	4.2
Non-irradiated	55	56.6	4.2
HPK W37 4x10 ¹⁴ n _{eq} /cm ²	Bulk	Gain Layer	
No annealed	51.6	53.1	4.1
120 min	44	58.4	4.8
180 min	43	61.7	4.2
1530 min	42.8	62.7	4.3
3930 min	42.2	48	4.1
24090 min	42.2	49.6	4
Non-irradiated	42.2	48	4
HPK W37 15x10 ¹⁴ n _{eq} /cm ²	Bulk	Gain Layer	
No annealed	27.3	~	4.4
120 min	26.6	30.5	5
180 min	26.6	30.5	5
1530 min	26.4	29.7	4.8
3930 min	26.4	29.2	4.7
24090 min	26.4	29.8	3.9
Non-irradiated	51.7	52.9	4.1

CONCLUSIONS

From the results of the characterization it can be concluded first, that the HPK samples behave more stable after neutron and proton irradiation, all the detectors from HPK presented low variations in their capacitance amplitude values and smooth curves. However, it can be observed that the non irradiated HPK samples have higher values for bulk and GL full depletion voltages than the values presented by the irradiated samples indicating a loss in charge recollection from the detector by dopant displacement without generating a large number of defects or radical defect clusters that may trap carriers. It can be appreciated that the HPK samples start to lose their GL integrity with the increase of irradiation behaving more like a PIN diode when the levels reach $6.5 \times 10^{14} \text{ p/cm}^2$ ($25 \times 10^{14} n_{eq}/\text{cm}^2$) but even at that values of irradiation, their acceptor removal coefficient is relatively close to the order of magnitude of radiation tolerant detectors..

FBK samples seem to be less resistant to radiation than HPK samples as they lose acceptors faster at lower irradiation fluence values. The presence of thermal donors inside the FBK samples changes their capacitance values when irradiated affecting considerably the measurements of the samples. For further radiation hardness analysis, a mechanism for electron isolation inside the bulk is recommended to analyze these samples as an n⁺-in-n detector. FBK samples showed good stability results at TCT station and some improvement in the bulk and GL integrity after annealing. Annealing for these samples is not recommended for longer periods than one week.

REFERENCES

- [1] QuantumFracture(2020).*LHC:Para que ha servido?*[online video] Available at:www.youtube.com/watch?v=U8uDRNj8Trg[Accessed 04/04/2021]
- [2] The Higgs Boson, CERN home page, Switzerland. <https://home.cern/science/physics/higgs-boson>, 2021.[Online; accessed 07/02/2021]
- [3] Herve A., The CMS detector magnet. *IEEE transactions on applied superconductivity*, 10 (1): 389-394, 2000.
- [4] CMS detector slice, CERN page, Switzerland. <http://cds.cern.ch/record/2120661/files/>, 2021.[Online; accessed 07/02/2021]
- [5] Foudas C., The CMS Level-1 trigger at LHC and Super-LHC. *In International conference for HEP in Philadelphia Pensilvania*. 2008. Available: <https://cds.cern.ch/record/2232067/files/arXiv:0810.4133.pdf>
- [6] Identifying tracks, CERN home page, Switzerland. <https://cms.cern/detector/identifying-tracks>, 2021.[Online; accessed 07/02/2021]
- [7] Interim summary report on the analysis of the 19 september 2008 incident at the LHC, 2008. Access: https://edms.cern.ch/ui/file/973073/1/Report_on_080919_incident_at_LHC__2_.pdf
- [8] The HL-LHC project, High Luminosity LHC project, CERN home page, Switzerland. <https://hilumilhc.web.cern.ch/content/hl-lhc-project>, 2021[Online; accessed 08/02/2021]
- [9] HL-LHC Industry, project schedule, 2021. Access: <https://project-hl-lhc-industry.web.cern.ch/content/project-schedule>
- [10] The Phase-2 Upgrade of the CMS Tracker, Technical design report, 2017. Access: <http://cds.cern.ch/record/2272264/files/CMS-TDR-014.pdf>
- [11] Presentation “Pileup Mitigation at the HL-LHC” [Online], 2014. Access: <http://cds.cern.ch/record/1957370/files/ATL-PHYS-SLIDE-2014-753.pdf>
- [12] Presentation “The Upgrade of the CMS Tracker for Super -LHC”,2009. Access: <https://slideplayer.com/slide/17577160/>

- [13] Nikita Kramarenko. Medical Imaging Applicability Study of Silicon Pixel Detectors with PSI46dig ROC. Master's Thesis, Lappeenranta University of Technology, Finland, 2020.
- [14] The CMS Phase-1 Pixel Detector Upgrade, 2020. Access: [Arxiv.org/pdf/2012.14304.pdf](https://arxiv.org/pdf/2012.14304.pdf)
- [15] Frank Hartmann. *Evolution of Silicon Sensor technology in Particle Physics*. Cham, Switzerland: Springer International Publishing AG, 2009.
- [16] A MIP Timing Detector for the CMS Phase-2 Upgrade, Technical design Report. Access: <https://cds.cern.ch/record/2667167/files/CMS-TDR-020.pdf>
- [17] Presentation "Status of the CMS pixel project", 2007. Access: <http://slideplayer.com/slide/4638787>
- [18] CMS Tracker detector performance results, CERN twiki, Switzerland. <https://twiki.cern.ch/twiki/bin/view/CMSPublic/DPGResultsTRK>, 2010.[Online; accessed 20/04/2021]
- [19] Mersi Stefano. Phase-2 upgrade of the CMS Tracker. *Nuclear and Particle Physics Proceedings*, 273-275: 1034-1041, 2016.
- [20] Sigmund Peter. Low-Speed limit of Bohr's stopping-power formula. *Physical Review A*, 54(4): 1-7, 1996.
- [21] Grigorii Pogudin. Characterization of Low Gain Avalanche Detectors for the CMS Experiment. Master's Thesis, Lappeenranta University of Technology, Finland, 2020.
- [22] Arto Javanainen. Particle radiation in microelectronics. PhD thesis, University of Jyväskylä, Finland, 2012.
- [23] Conell SH. Particle interactions with matter, lecture. The African School of Physics ASP2012, 2012.[Online]. Access: <https://indico.cern.ch/event/145296/contributions/1381063/attachments/136866/194145/Particle-Interaction-Matter-upload.pdf>
- [24] Landau distribution for ionizing particles, Stefano Meroli Life of an Engineer at Cern, CERN home page, Switzerland.

https://meroli.web.cern.ch/lecture_landau_ionizing_particle.html, 2021.[Online; accessed 25/04/2021]

[25] Porter, L.E. The Barkas-Effect to Bethe-Bloch Stopping Power. *Advances in Quantum Chemistry, Academic Press*, 46(2): 91-119, 2004.

[26] Guesmia A., Msimanga M., Mtshali C.B., Pineda-Vargas C.A. and Nkosi M. Readjustment of the Bohr stopping force from energies of keV/n to a few tens of MeV/n ions in elemental targets. *Physics Letters A*, 384(31):126794, 2020.

[27] The straggling function . Energy loss distribution of charged particles in silicon layers, Stefano Meroli Life of an Engineer at Cern, CERN home page, Switzerland. 2021. https://meroli.web.cern.ch/lecture_StragglingFunction.html[Online; accessed 25/04/2021]

[28] Karoui A., Rozgonyi G., and Ciszek T. Effect of oxygen and nitrogen doping on mechanical properties of silicon using nanoindentation. *MRS proceedings*. 821:8-36, 2004.

[29] Development of radiation hard detectors – differences between Czochralski silicon and float zone silicon, internal report, 2003. Access: <https://aalto.fi/bitstream/handle/123456789/2117/isbn9512267411.pdf?sequence=1&isAllowed=y>

[30] Manzari V. Silicon detectors, semiconductor detectors, signal, noise and electronics, lecture. The 5th Egyptian School on High Energy Physics ESHEP2015, 2015.[Online]. Access:https://indico.cern.ch/event/453690/sessions/99350/attachments/1184199/1726998/2015-11_SiliconDetectors_manzari_Lecture2.pdf

[31] Mihail E. Levinshtein and Grigorii S. Simin. Barrieri ot kristalla do integralnoi shemi. Saint-Petersburg: Biblioteka Quant, 1988.

[32] Krammer M. and Hartmann F. Silicon detectors, lecture. Excellence in Detectors and Instrumentation Technologies EDIT2011, 2011. [Online]. Access: <https://indico.cern.ch/event/124392/contributions/1339904/attachments/74582/106976/IntroSilicon.pdf>

[33] PIN-diodes, radartutorial <https://www.radartutorial.eu/21.semiconductors/hl14.en.html>, [Online; accessed 15/02/2021]

- [34] Ramirez-Jimenez F.J., PIN diode detectors. American Institute of Physics Conference Proceedings 1026, 213-226, 2008.
- [35] Gregor Kramberger. Signal development in irradiated silicon detectors. PhD thesis, University of Liubljana, Eslovenia, 2001.
- [36] Moffat N., Bates R., Bullough M., Flores L., Maneuski D., Simon L., Tartoni N., Doherty F., and Ashby J. Low gain avalanche detectors (LGAD) for particles physics and synchrotron applications. In *Journal of Instrumentation, 11th International conference on position sensitive detectors*. Pages 1-12, 2017.
- [37] Semiconductor fundamentals, carrier recombination and generation. Access: http://ecee.colorado.edu/~bart/ecen3320/newbook/chapter2/ch2_8.htm
- [38] Sze S.M. Semiconductor devices: Physics and technology. United States of America: John Wiley & Sons Inc., 2nd edition, 2002.
- [39] Cortes I., Fernandez-Martinez P., Flores D., Hidalgo S. and Rebollo J. Gain of RT-APD devices by means of TCAD numerical simulations. In *Proceedings of the 8th Spanish conference on electron devices (CDE'2011)*. 2011.
- [40] Sadrozinski H.F.-W., Anker A., Chen J., Fadeyev V., Freeman P., Galloway Z., Gruey B., Grabas ., Jhon C., Liang Z., Losakul R., Mak S.N., Seiden A., Woods N., Zatserklyaniy A., Baldassarri B., Cartiglia N., Cenna F. and Zavrtanik M. Ultra-fast silicon detectors (UFSD). *Nuclear instruments and Methods in Physics Research Section A: Accelerators, Spectrometers, Detectors and Associated Equipment*. 831
- [41] Cartiglia N., Arcidiacono R., Borghi G., Boscardin M., Costa M., Galloway Z., Fausti F., Ferrero M., Ficorella F., Mandurrino M., Mazza S., Olave E.J., Paternoster G., Siviero F., Sadrozinski H.F.-W., Sola S., Staiano A., Seiden A., Tornago M. and Zhao Y. LGAD designs for future particle trackers. *Nuclear Instruments and Methods in Physics Research Section A: Accelerators, Spectrometers, Detectors and Associated Equipment*. 979:164383, 2020.
- [42] Presentation “Detector requirements for future high-energy collider experiments “, 2020. Access: https://indico.cern.ch/event/813597/contributions/3727952/attachments/1988376/3314100/EvaSicking_DetectorRequirements.pdf

- [43] Presentation “Time resolution of ultra-fast ilicon detectors (thin LGAD)”.Access: <https://indico.cern.ch/event/577879/contributions/2740418/attachments/1575077/2487327/HSTD1--HFWS1.pdf>
- [44] Cartiglia N., Dellacasa G., Garbolino S. & Marchetto F., Rivetti A., Arcidiacono R., Obertino M., Fadeyev V., Sadrozinski H.F-W., Seiden A., Zatserklyaniy N., Bellan R., Cenna F., Monaco V., Picerno A., Sacchi, F., Solano A., Pellegrini G., Fernández-Martínez P., Quirion D., Timing Capabilities of Ultra-Fast Silicon Detectors. *Acta Physica Polonica B Proceedings Supplement*. 7, P. 657, 2014.
- [45] Presentation “Timing capabilities of ultra-fast silicon detectors”, 2014. Access: <https://slideplayer.com/slide/10779114/>
- [46] Shudhashil Bharthuar. Prototype evaluation of silicon sensors and other detector components suitable for future CMS Tracker. Master’s thesis, University of Helsinki, Finland, 2019.
- [47] Eremin V., Li Z. and Iljashenko I.. Trapping induced N,ff and electrical fieldtransformation at different temperatures in neutron irradiated high resistivitysilicon detectors. *Nuclear Instruments and Methods in Physics*, 1995.
- [48] Kramberger G., Cindro V., Mandic I., Mikuz M. and Zavrtanik M. Effective trapping time of electrons and holes in different silicon materials irradiated with neutrons, protons and pions . *Nuclear Instruments and Methods in Physics Research Section A: Accelerators, Spectrometers, Detectors and Associated Equipment*. 481 (1-3):297-305, 2002.
- [49] Cristea M., Capacitance-voltage profiling techniques for characterization of semiconductor materials and devices. *University of Bucharest*. [Online]. Access: <https://arxiv.org/pdf/1011.3463.pdf>
- [50] Presentation “Effect of thermal donors induced in bulk and variation in p-stop dose on the no-gain distance measurements of LGADs”, 2020. Access: https://indico.cern.ch/event/895924/contributions/3993229/attachments/2115002/3560057/Vertex_Shudhashil_CMS_poster_oralpresentation.pdf
- [51] Bharthuar, S., Ott J., Helariutta K., Litichevskyi V., Brücken E., Gädda A., Martikainen L., Kirschenmann S., Naaranoja T., Luukka P. Study of interpad-gap of HPK

3.1 production LGADs with Transient Current Technique. *Nuclear Instruments and Methods in Physics Research, Section A: Accelerators, Spectrometers, Detectors and Associated Equipment A.* 979:164494, 2020.